Spectral reflectance "deconstruction" of the Murchison CM2 carbonaceous chondrite and implications for spectroscopic investigations of dark asteroids

Edward Cloutis, Valerie Pietrasz, Cain Kiddell, Matthew Izawa, Pierre Vernazza, Thomas Burbine, Francesca Demeo, Kimberly Tait, James Bell, Paul Mann, et al.

Spectral reflectance "deconstruction"of the Murchison CM2 carbonaceous chondrite and implications for spectroscopic investigations of dark asteroids

Edward A. Cloutis[a], Valerie B. Pietrasz[b], Cain Kiddell[a], Matthew R.M. Izawa[a,c] , Pierre Vernazza[d], Thomas H. Burbine[e], Francesca DeMeo[f], Kimberly T. Tait[g], James F. Bell III[h], Paul Mann[a], Daniel M. Applin[a], Vishnu Reddy[i]

a Department of Geography, University of Winnipeg, 515 Portage Avenue, Winnipeg R3B 2E9, Manitoba, Canada
b Division of Geological and Planetary Sciences, California Institute of Technology, 1200 East California Boulevard, Pasadena, CA 91125, United States
c Institute for Planetary Materials, Okayama University, 827 Yamada, Misasa, Tottori 682-0193, Japan
d Aix Marseille Université, CNRS, LAM, Laboratoire d'Astrophysique de Marseille, Marseille, France
e Department of Astronomy, Mount Holyoke College, South Hadley, MA 01075, USA
f Department of Earth, Atmospheric, and Planetary Sciences, Massachusetts Institute of Technology, 77 Massachusetts Avenue 54-416, Cambridge, MA 02139, USA
g Royal Ontario Museum, 100 Queen's Park, Toronto M5S 2C6, ON, Canada
h School of Earth and Space Exploration, Arizona State University, Box 876004, Tempe, AZ 85287-6004, USA
i Lunar and Planetary Laboratory, University of Arizona, 1629 East University Boulevard, Tucson, AZ 85721-0092, USA

Carbonaceous chondrites (CCs) are important materials for understanding the early evolution of the solar system and delivery of volatiles and organic material to the early Earth. Presumed CC-like asteroids are also the targets of two current sample return missions: OSIRIS-REx to asteroid Bennu and Hayabusa-2 to asteroid Ryugu, and the Dawn orbital mission at asteroid Ceres. To improve our ability to identify and characterize CM2 CC-type parent bodies, we have examined how factors such as particle size, particle

packing, and viewing geometry affect reflectance spectra of the Murchison CM2 CC. The derived relationships have implications for disc-resolved examinations of dark asteroids and sampleability. It has been found that reflectance spectra of slabs are more blue-sloped (reflectance decreasing toward longer wavelengths as measured by the 1.8/0.6 μm reflectance ratio), and generally darker, than powdered sample spectra. Decreasing the maximum grain size of a powdered sample results in progressively brighter and more red-sloped spectra. Decreasing the average grain size of a powdered sample results in a decrease in diagnostic absorption band depths, and redder and brighter spectra. Decreasing porosity of powders and variations in surface texture result in spectral changes that may be different as a function of viewing geometry. Increasing thickness of loose dust on a denser powdered substrate leads to a decrease in absorption band depths. Changes in viewing geometry lead to different changes in spectral metrics depending on whether the spectra are acquired in backscatter or forward-scatter geometries. In backscattered geometry, increasing phase angle leads to an initial increase and then decrease in spectral slope, and a general decrease in visible region reflectance and absorption band depths, and frequent decreases in absorption band minima positions. In forward scattering geometry, increasing phase angle leads to small non-systematic changes in spectral slope, and general decreases in visible region reflectance, and absorption band depths. The highest albedos and larger band depths are generally seen in the lowest phase angle backscattering geometry spectra. The reddest spectra are generally seen in the lowest phase angle backscatter geometry spectra. For the same phase angle, spectra acquired in forward scatter geometry

are generally redder and darker and have shallower absorption bands than those acquired in backscatter geometry. Overall, backscatter geometry-acquired spectra are flatter, brighter, and have deeper 0.7 μm region absorption band depths than forward scatter geometry-acquired spectra. It was also found that the 0.7, 0.9, and 1.1 μm absorption bands in Murchison spectra, which are attributable to various Fe electronic processes, are ubiquitous and can be used to recognize CM2 chondrites regardless of the physical properties of the meteorite and viewing geometry.

1. Introduction

Carbonaceous chondrites (CCs) are among the most useful meteorites for addressing issues related to the formation, history, and dynamics of the early solar system, the delivery and distribution of water in the solar system, and prebiotic chemistry relevant to the origin and evolution of life on Earth. A major driver of spectral reflectance studies of CCs is for establishing linkages between CCs and specific parent bodies. The importance of this is underscored by the fact that potential CC asteroidal parent bodies are the targets of two current sample return missions: OSIRIS-REx to asteroid (101955) Bennu (1999 RQ_{36}) (Lauretta, 2015), and Hayabusa-2 to asteroid (162173) Ryugu (1999 JU_3) (Tsuda et al., 2013). Determining the surface mineralogy and physical properties of the dark asteroids targeted for sample return prior to the encounters can help to select sampling sites of highest scientific value and sampleability, as well as understand the evolution of these bodies (e.g., whether they are rubble piles or intact fragments).

Available Earth-based spectroscopic data for both Bennu and Ryugu are uncertain in terms of their mineralogies and whether spectrally diagnostic features may be present. For instance, 0.4–2.5 μm telescopic spectra of Bennu appear to lack absorption features (Binzel et al., 2002, 2015; Clark et al., 2011); however weak absorption bands are allowed by the signal-to-noise ratio of the data. For asteroid Ryugu, most of the observational data suggest that it is spectrally featureless, although some reflectance spectra show weak, and sometimes persistent, minor absorption bands (Binzel et al., 2002; Lazzaro et al., 2013; Moskovitz et al., 2013), and one set of observations suggest the presence of absorption features that are consistent with CM2 chondrites (Vilas, 2008).

Spectroscopic properties of CCs are also important for understanding the nature of dark materials on the surface of Vesta (e.g., McCord et al., 2012; Nathues et al., 2014) and the surface composition of asteroid Ceres (e.g., Chapman and Salisbury, 1973; McCord and Gaffey, 1974; Lebofsky, 1978; De Sanctis et al., 2015; Ammannito et al., 2016), both of which are primary targets of the Dawn spacecraft (Russell and Raymond, 2011). CM-type material has been invoked as a leading candidate for the dark material that is widespread on the surface of Vesta (Nathues et al., 2014; Palomba et al., 2014). This is consistent with the presence of CM-like xenoliths in HED meteorites that are presumed to originate from Vesta (Cloutis et al., 2011b, and references therein). In some howardites, the CM-like material can comprise the majority of the sample (e.g., PRA 04401: McCoy and Reynolds, 2007; Herrin et al., 2010, 2011).

In addition to dedicated spacecraft missions, dark, presumed carbonaceous, asteroids are also common and scientifically important targets for telescopic observations, including those in the main asteroid belt and in near-Earth space (e.g., Popescu et al., 2011; Izawa et al., 2015; Takir et al., 2015).

CM carbonaceous chondrites are the most common class of hydrated CCs, representing 1.5% of meteorite falls (carbonaceous chondrites represent < 4% of all falls; Norton, 2002). They generally exhibit different degrees of (probable) post-accretional aqueous alteration, with petrologic grades ranging from ~1 to ~3 (Grady et al., 1987; McBride et al., 2002; Trigo-Rodriguez et al., 2006; Rubin et al., 2007; Righter, 2008; de Leuw et al., 2009). A number of CM-type meteorites also show evidence of post-aqueous thermal alteration (Cloutis et al., 2012b, and references therein). CM2 chondrites consist largely of ferromagnesian phyllosilicates, followed by anhydrous silicates (olivine, pyroxene), and minor components (present at the few percent level) that include magnetite, Fe-sulphides, Ca–Mg–Fe carbonates, and organic material (e.g., Brearley and Jones, 1998; Bland et al., 2004; Zolensky et al., 2008; Howard et al., 2009).

In addition to the CM2 meteorites being a well-defined group, CM2-type materials are common as xenolithic material in other types of meteorites, including ordinary chondrite breccias, howardites, lunar samples, and others (e.g., Buchanan et al., 1993; Zolensky et al., 1996; Gounelle et al., 2003).

Reflectance spectra of CM chondrites are characterized by a ubiquitous series of absorption features near 0.75, 0.9, and 1.1 μm, that are attributable to phyllosilicate Fe^{2+}-Fe^{3+} charge transfers (0.75 μm band) or Fe^{2+} crystal field transitions (0.9 and 1.1 μm bands) (Clark et al., 1990). For $Fe^{2+}Fe^{3+}$-bearing phyllosilicates, the 0.9 and 1.1 μm bands will appear together (Cloutis et al., 2011b). Phyllosilicates, primarily Fe-bearing serpentine and cronstedtite (an Fe^{3+}-Fe^{2+}-bearing phyllosilicate), are the most common phase in CMs, comprising ~65–85 vol%, and with serpentine/cronstedtite ratios varying between different CMs (Bland et al., 2004, 2008; Howard et al., 2008, 2009, 2010a, 2010b). Absorption bands attributable to these phases are seen in CM reflectance spectra, and hence s are indicative and characteristic of these phases in hydrated CCs (such as CMs). In particular, the 0.7 μm absorption feature appears to be nearly exclusively confined to CM chondrites (Cloutis et al., 2011b). CM-type chondrites that have been subsequently thermally metamorphosed (termed ATCCs: Aqueously altered and Thermally metamorphosed Carbonaceous Chondrites) may continue to exhibit these absorption features, albeit generally with their depths decreasing with increasing thermal metamorphism (Cloutis et al., 2012b).

Other hydrated CCs, such as CI1 chondrites, do not, or rarely, display such bands because their more pervasive aqueous alteration leads to the production of more Mg-rich phyllosilicates (Howard et al., 2010a, 2010b). In CI1 reflectance spectra, when the 0.7 μm phyllosilicates band is present, it is usually located at shorter wavelengths (< 0.7 μm) than the corresponding absorption bands in CM2 chondrites (> 0.7 μm; Cloutis et al., 2011a). The cause of this difference is unknown, but likely relates to structural differences between the major phyllosilicates in CIs (saponite + serpentine) versus CMs (serpentine + cronstedtite) (Bland et al., 2004, 2008; Howard et al., 2009, 2010a, 2010b, 2015).

CR chondrites also include some hydrated members (Cloutis et al., 2012a) and their spectra rarely display the 0.75, 0.9, and 1.1 μm absorption bands, either because of: (1) lower degrees of aqueous alteration (resulting in lower production of phyllosilicates) (Bland et al., 2008), or because their phyllosilicates may be more Mg-rich than those in CM2s, perhaps due to differences in pre-aqueous compositions between CRs and CMs (Noguchi, 1995). Other ungrouped, aqueously altered CCs, such as Tagish Lake (petrologic grade ~2) also do not exhibit these absorption bands,

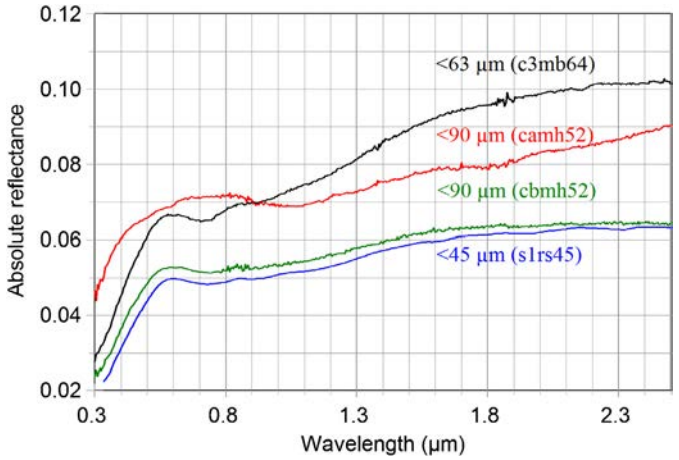

Fig. 1. Some previously-measured reflectance spectra of the Murchison CM2 carbonaceous chondrite from the RELAB archive (RELAB sample IDs and grain size of each spectrum are indicated). All spectra were measured at $i = 30°$ and $e = 0°$.

or show them only weakly ($<<1\%$ deep) (Izawa et al., 2015), likely because of abundant opaques (Cloutis et al., 2012c).

Among the various taxonomic classes of dark asteroids (e.g., Bus and Binzel, 2002; DeMeo et al., 2009), the Cgh/Ch group is uniquely defined as possessing an absorption band in the 0.7 μm region. This feature is nearly ubiquitous in CM2 reflectance spectra (Cloutis et al., 2011b; Vernazza et al., 2016), and largely absent from reflectance spectra of other CC groups, as discussed above. A number of specific asteroids show one or more absorption features attributable to Fe-bearing phyllosilicates, which is most consistent with CM2 chondrites (e.g., Vilas and Gaffey, 1989; Cloutis et al., 2011b, and references therein; Vernazza et al., 2016). Consequently, the parent body/bodies of the CM chondrites are generally thought to reside within the Ch and Cgh taxonomic asteroid group (Vilas and Gaffey, 1989; Vilas et al., 1993; Lantz et al., 2013; Burbine, 2014; Rivkin et al., 2015; Vernazza et al., 2016). These two asteroid taxonomic types represent ~10% of the mass of the asteroid belt (Rivkin, 2012; DeMeo and Carry, 2013) and can be found at all heliocentric distances within the asteroid belt. They also represent about 10% of the near-Earth asteroid population (Stuart and Binzel, 2004; Binzel et al., 2004).

The spectral reflectance properties of CM chondrites are diverse and not all of the factors that may affect their reflectance spectra have been thoroughly studied. Cloutis et al. (2011b) found that CM2 chondrites can show diverse spectral behavior in terms of overall reflectance, spectral slopes, and strengths of phyllosilicate-associated absorption bands. It is suspected that some of this spectral diversity may relate to the fact that many CM chondrites are breccias (Hanowski and Brearley, 2000), and hence different subsamples could have different spectral properties depending on their mineralogy. Other studies have shown that other properties and parameters, such as viewing geometry and grain size can also change CM spectral properties (e.g., Johnson and Fanale, 1973; Cloutis et al., 2011b). Even spectral reflectance measurements of a single carbonaceous chondrite (e.g., Murchison) can show spectral diversity that cannot be attributed to factors such as particle size and spectral measurement techniques (e.g., Fig. 1). Different fine-grained powders ($<45, <63, <90$ μm) of Murchison, some of which presumably sample different portions of Murchison, show differences in absolute reflectance, spectral slope, and absorption band strengths in the 0.6–1.3 μm region. Many of these differences, or their magnitudes, would not be seen in a homogeneous sample. Physical and observational properties might account for spectral differences between CM chondrites and presumed parent bodies, such as the position of 0.7 μm region absorption features (Burbine, 1998; Fornasier et al., 2014).

To better understand the factors that affect the spectral reflectance properties of carbonaceous chondrites, and specifically CM chondrites, we undertook a systematic 0.35–2.5 μm spectral reflectance study of how factors such as possible sample heterogeneity, whole rock versus powders, particle size distribution and range, packing density/porosity, and viewing geometry can affect reflectance spectra of a specific CM2 carbonaceous chondrite (Murchison). These data were supplemented with other reflectance spectra of Murchison available from other sources. It should be noted that different types of carbonaceous chondrites can also be distinguished at longer wavelengths, using features such as the 3 μm region OH/H_2O absorption band and silicate emission features in the 8–20 μm region (e.g., Miyamoto, 1987; Miyamoto and Zolensky, 1994; Takir et al., 2013). The 3 μm band likely provides an additional means to recognize CM-type chondrites. Typically a third of C-type asteroids do show the presence of a 0.7 μm absorption feature (Rivkin, 2012), and its presence strongly correlates with presence of a 3 μm absorption band (e.g., Vilas, 1994), but the presence of a 3 μm band does not necessarily imply that a 0.7 μm band will also be present.

2. Methods

This study focused on three contiguous saw-cut chips totalling 10 g of the Murchison meteorite held at the Royal Ontario Museum (ROM #M52364), supplemented with saw-cut fines of this sample, two unsorted powder samples containing some larger (~1–3 mm diameter) fragments (one fragment exhibiting partial fusion crust) from the University of North Dakota (Gaffey, 1976), three powder samples of different grain sizes from Arizona State University, various digitally-available Murchison spectra from the RELAB archive (http://planetary.brown.edu/relab/; Cloutis et al., 2011b), a powdered sample spectrum from Gillis-Davis et al. (2015), and from other previously-published studies (Johnson and Fanale, 1973; Gaffey, 1974; Salisbury et al., 1975; Miyamoto et al., 1982, 2000; Calvin et al., 1999). Sample descriptions and reflectance spectra included in this study are provided in Table 1.

The analytical procedure for the ROM Murchison chips was to first spectrally characterize spots on their exterior and interior surfaces. Selected subsamples were then extracted and crushed by hand in an alumina mortar and pestle and dry sieved to obtain various grain size fractions, as described below. Dry sieving consisted of gently brushing the crushed powder in a stainless steel sieve of the required size with a soft brush in order to remove adhering fines and without contaminating or inadvertently altering the sample through wet sieving.

Reflectance spectra were measured with an Analytical Spectral Devices FieldSpec Pro HR spectrometer that acquires data from 0.35 to 2.50 μm, with a spectral resolution between 2 and 7 nm and spectral sampling interval of 1.4 nm. The data are internally re-sampled by the instrument to output data at a uniform wavelength spacing of 1 nm. Data below approximately 0.4 μm may be affected by low signal levels and hence data in the 0.35–0.40 μm region, particularly abrupt changes in slope, are suspect. Some spectra may also show small and narrow absorption bands in the 0.62–0.65 μm region, which are due to artefacts from the spectrometer's order-sorting filter. The ASD spectrometer consists of three detectors, with changeovers at 1.00 and 1.83 μm. Due to differences in each detector's response across their respective wavelength ranges and decreasing light intensity toward longer wavelengths, signal to noise varies in different wavelength regions – the spectra are generally noisier toward longer wavelengths and at the ends of each detector's range. Incident light was provided by an in-house 100 W quartz-tungsten-halogen collimated light

Table 1
Description of Murchison samples and spectra included in this study.

Original sample ID	PSF sample ID	Description	Source
Me-2641(a)	MJG009	~400 mg fine powder	[1]
Me-2641(b)	MJG226	2.6 g: 2 fragments + abraded powder	[1]
MUR >150 μm	JFB21	>150 μm powder	[2]
MUR #5377	JFB22	coarse-grained powder	[2]
MUR crushed 5/21/77	JFB23	fine-grained powder	[2]
M252364	M52364-a	Three saw-cut pieces; 10.39 g total	[3]
M252364	M52364-b	"Clean" saw cut powder; 1.76 g	[3]
M252364	M52364-c	"Contaminated" saw cut powder; 7 g	[3]

Reflectance spectra of Murchison samples measured at PSF:

MJG009	< 150 μm; two spectra (sample repacked and remeasured): 090817b.004, 005
MJG226	Two chip face spectra (chip repositioned and remeasured): 091118a.001, 002
JFB23	< 90 μm (mix of < 45 and 45–90 μm powders), various phase angles: 140620b.001-009
JFB22 + 23	Mix of various proportions of < 45 + 500–1000 μm powders: 140721b.001-0.024 (each sample repacked and remeasured)
M52364-a	16 spots on saw cut faces and 12 spots on fusion crust: 040616a.001-028
M52364-a	Six subsamples, < 150 μm (each sample repacked and remeasured): 040702a.001-012
M52364-a	1 subsample, progressively crushed and measured at each sieving step (each sample repacked and remeasured): < 1000, < 500, < 250, < 90, < 45 μm: 140703a.001-012
M52364-a	1 < 90 μm subsample measured as loose, regular, and tamped powder: 140708a.001, 003, 005
M52364-b	"Clean" saw-cut fines; one spectrum: 150409a.005
M52364-c	"Contaminated" saw-cut fines; one spectrum: 150409a.006

Reflectance spectra of Murchison samples from RELAB archive

RELAB ID	Grain size	*i*°, *e*°; spectral range; spectral resolution
c2mb64	< 125 μm	30/0; 0.3–2.6 μm; 5 nm
c3mb64	< 63 μm	30/0; 0.3–2.6 μm; 5 nm
c4mb64	63–125 μm	30/0; 0.3–2.6 μm; 5 nm
camh52	< 90 μm	30/0; 0.3–2.6 μm; 5 nm
cbmh52	< 90 μm	30/0; 0.3–2.6 μm; 5 nm
ccmh52	< 180 μm	30/0; 0.3–2.6 μm; 5 nm
mgp094[a]	< 150 μm	integrating sphere; 0.35–2.525 μm; 5 nm
cdms02	< 200 μm	30/0; 0.35–2.6 μm; 5 nm
cbms02	100–200 μm	30/0; 0.35 to > 2.6 μm; 5 nm
ccms02	100–200 μm	30/0; 0.35–2.6 μm; 5 nm
cems02	100–200 μm, olivine enriched	30/0; 0.35–2.6 μm; 5 nm
cfms02	100–200 μm, olivine-enriched	30/0; 0.35–2.6 μm; 5 nm
cgms02	< 40 μm, olivine-enriched	30/0; 0.35–2.6 μm; 5 nm
cmms02	100–200 μm, matrix-enriched	30/0; 0.35 to > 2.6 μm; 5 nm
cnms02	100–200 μm, matrix-enriched	30/0; 0.35–2.6 μm; 5 nm
coms02	< 40 μm, matrix-enriched	30/0; 0.35–2.6 μm; 5 nm
s1rs45	≤ 45 μm	30/0; 0.335 to ≥ 2.6 μm; 5 nm

Reflectance spectra of Murchison from previous studies

Grain size	Viewing geometry	Source
< 150 μm (3 spectra)	integrating sphere	[4]
< 150 μm	$i = 30°$, $e = 0°$	[5]
< 46 and < 1190 μm	integrating sphere	[6]
< 100 μm	$i = 30°$, $e = 30°$	[7]
< 74 μm	integrating sphere	[8]
< 63 μm pressed pellet	$i = 30°$, $e = 0°$	[9]
< 74, 74–147, 147–495 μm	integrating sphere	[10]
74–147 μm fractions[b]	integrating sphere	[10]

Source of samples or data: [1] Gaffey (1976). [2] Arizona State University. [3] Royal Ontario Museum. [4] Gaffey (1974). [5] Gillis-Davis et al. (2015). [6] Miyamoto et al. (1982). [7] Miyamoto et al. (2000). [8] Salisbury et al. (1975). [9] Matsuoka et al. (2015). [10] Johnson and Fanale (1973).

[a] Original Gaffey (1976) spectrum.

[b] Fractions enriched or depleted in red/orange-colored grains.

source. Both the light source and the spectrometer fiber optic assembly were mounted on goniometer arms in order to be able to independently vary the phase angle *p*, the angle subtended by the lines from light source to target and from target to detector. The phase angle is the sum of the incidence angle *i* (the angle between a normal to the surface and the light source to the sample surface) and emission angle *e* (the angle between a normal to the surface and the surface to detector line). An emission angle of zero is equivalent to nadir-looking geometry perpendicular to the sample surface, and non-zero angles are measured from nadir. If *i* and *e* are both listed as positive this indicates that they are located on either side of the surface normal (forward scattering geometry). A negative value for *e* indicates that both *i* and *e* are on the same side of the surface normal (backscattering geometry).

Sample spectra were measured relative to a NIST-traceable Spectralon® (Labsphere, North Sutton, NH) standard and corrected for minor (less than ~2%) irregularities in its absolute reflectance. In each case, 500 spectra of the dark current, standard, and sample were acquired and averaged, to provide sufficient signal-to-noise for subsequent interpretation. Ordinarily, sample powders were poured into machined aluminium sample cups and the surface gently smoothed by drawing the edge of a clean glass microscope slide across the surface to minimize surface topography and compaction.

Various spectral metrics were derived to characterize changes in reflectance spectra associated with the different sample variables that were investigated. These include depths of absorption bands in the 0.75, 0.9, and 1.1 μm region (using Eq. 32 of Clark and Roush, 1984: band depth = 1 – (reflectance at the band center divided by reflectance of the continuum at the same wavelength as the band center)), and wavelength position (center) of these absorption bands after continuum removal, which involved dividing the spectrum by a straight line continuum tangent to each spectrum across the ~0.56–1.35 μm interval. One tangent point was located on the visible region reflectance maximum while the other was fixed at 1.35–1.38 μm to avoid any OH/H_2O absorption bands in this region. Other metrics include spectral slopes (IR slope (also termed spectral slope): as measured by the 1.8/0.6 μm reflectance ratio; visible slope: as measured by the 0.56/0.40 μm reflectance ratio), and albedo (absolute reflectance at 0.56 μm). The sample spectra and the spectral metrics for the samples included in this study are provided in the *on-line supplement*.

2.1. Sample preparation methods for textural variation study

2.1.1. Grain size series

A grain size series was created by repeated cycles of crushing and dry-sieving of a single ~1 g subsample of Murchison, with spectra measured at each step. The sample was crushed until it entirely passed through a particular sieve. A reflectance spectrum was measured, then the sample was crushed again until the entire sample passed through the finer sieve, its reflectance spectrum was measured, and the process was repeated. The sieve sizes used to constrain the maximum particle size were 1000, 500, 250, 150, 90, and 45 μm (Table 1). Each sample was spectrally characterized twice, with the sample cup emptied and repacked each time. It is possible that some mineralogical sorting may occur during this process, however, the effects of such sorting or selection are expected to be minor due to the overall fine grain size and preponderance of relatively homogeneous matrix material in Murchison. This procedure minimizes any subsample-to-subsample variations that may explain some of the spectral diversity seen in previous spectral reflectance studies of Murchison (Cloutis et al., 2011b).

These sample spectra were supplemented with reflectance spectra of saw-cut fines produced during cutting of the ROM's main piece of Murchison (1.3 kg) and polishing of the cut faces. The two saw-cut samples include "clean" fines gathered during the cutting process – the sample was dry-cut with a diamond wire saw – and a sample possibly contaminated with aluminum oxide and silicon carbide powders used during the smoothing process.

2.1.2. Porosity effects

Four kinds of particle porosity effects were examined. "Regular" samples were prepared by pouring the powder into a sample cup and leveling the surface with the edge of a clean glass slide. "Fluffy" samples consist of the regular sample stirred with a needle to create a less-dense sample. "Dense" samples were firmly compressed by hand using the face of a clean glass slide to simulate a compressed, indurated or otherwise compacted surface. "Airfall" samples were prepared by sprinkling the dense sample with < 90 μm powder passed through a steel sieve. Two thicknesses of coatings were produced: thin: where the underlying sample could still be seen, and heavier: where the underlying sample was no longer visible.

2.1.3. Coarse plus fine mixture spectra

The "coarse plus fine" mixture samples consist of coarse particles (500–1000 μm) to which were added various proportions of < 45 μm fine particles which were then mixed by shaking together in a sealed sample vial. The coarse and fine fractions are derived from the same Murchison sub-sample.

2.1.4. Slab/whole-rock spectra and intra-sample heterogeneity

Spots that were ~5 mm in diameter on both saw-cut interior and fusion-crusted surface of the three ROM Murchison samples were spectrally characterized. Images of the slabs and locations of the spot spectra and regions where subsamples were removed are shown in Fig. 2. After spot spectra were collected, ~500 mg of sample from each spot was chipped off the slab using a chisel and rotary cutting tool and powdered to < 150 μm particle size to investigate the extent of spectral homogeneity in different sub-samples of the same 'bulk' Murchison sample.

3. Results

Murchison, in common with almost all other CM2 chondrites, has low overall reflectance and resolvable absorption features centered near 0.75, 0.9, and 1.1 μm (Cloutis et al., 2011b). Most previous reflectance spectra of Murchison powders have 'red' spectral slopes (increasing reflectance with increasing wavelength). There is a marked change in spectral slope near 0.56 μm. The reflectance spectra of the various aspects of Murchison that were investigated are discussed below, along with the various spectral metrics.

3.1. Slab spectra

As mentioned, reflectance spectra were acquired for spots ~5 mm in diameter on various portions of the Murchison chips, including interior saw-cut surfaces and fusion crust-coated surfaces. Fusion crust spectra were included because they may provide insights into the spectral properties of asteroids with CM-like compositions which have been affected by short-term heating in an oxidizing environment, as may occur during impact heating on CM parent bodies, and to compare them with CM-like CCs that have been aqueously-altered and subsequently thermally metamorphosed (Cloutis et al., 2012b). A number of the spot spectra turned out to be unusable because of instrumental artefacts.

The saw-cut interior face spot spectra (Fig. 3a) show low albedo (< 5.5% at 0.56 μm) and the expected blue-sloped spectra (1.8/0.6 μm reflectance ratio < 1) (Johnson and Fanale, 1973). Absorption bands attributable to the sample's Fe-bearing phyllosilicates are present in the 0.7–1.2 μm region. These can be seen more clearly in the straight line continuum-removed spectra (Fig. 3b). Band depths in this region are on the order of 2.0–3.6%. The 0.7-μm region Fe^{3+}-Fe^{2+} charge transfer absorption band is apparent in the continuum-removed spectra near 0.73 μm, as is the 0.9 μm Fe^{2+} crystal field transition absorption band of Fe-bearing phyllosilicates located near 0.90 μm. A companion 1.1 μm region Fe^{2+} crystal field transition absorption band is also present but less evident because of increased noise in this region – it is best seen near 1.13 μm. All three bands are seen in the vast majority of CM reflectance spectra (Cloutis et al., 2011b). Absorption band positions show slight variability, but this is likely due to the broad and weak nature of the bands and such bands are sensitive to small differences in continuum slope. Differences in overall slope are likely attributable to differences in surface roughness (Harloff and Arnold, 2001).

Similar to the interior face spectra, the spot spectra of the fusion crust are also consistently blue-sloped (as expected for solid samples), but show no evidence of the 0.75-μm region Fe-phyllosilicate absorption band (Fig. 3c). The expected 0.9 and 1.1 μm absorption bands are not evident as two separate bands, rather they appear as a single broader band centered near 1.0–1.05 μm that is consistent with Fe-bearing glassy/amorphous materials (Horgan et al., 2014) or magnetite (Cloutis et al., 2011a,

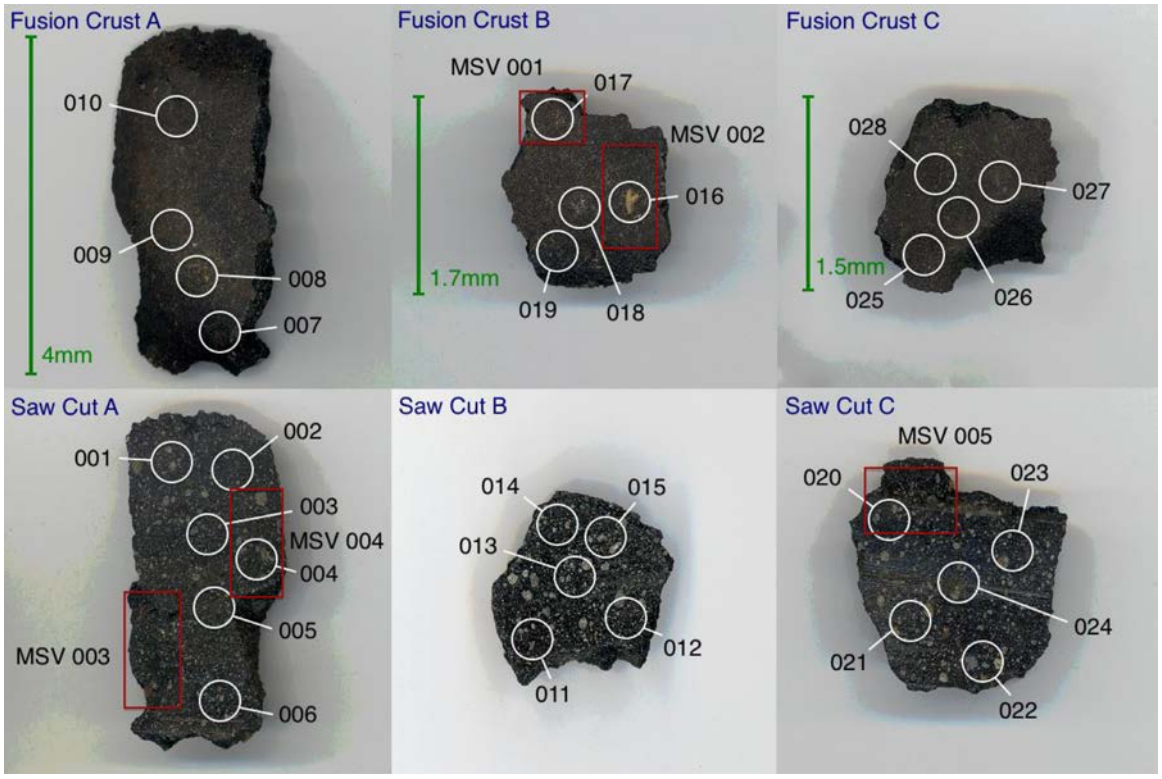

Fig. 2. Images of the main ROM Murchison subsamples used in this study along with locations of spot spectra (white circles) and of samples extracted for grain size spectral analysis (red rectangles). MSV006 (not shown) is a concentrate of the fusion crust from sample "Fusion Crust A" that was extracted from the uppermost part of the exterior surface. (For interpretation of the references to color in this figure legend, the reader is referred to the web version of this article).

2011b). There are also weak H_2O-associated absorption bands in the 1.4 and 1.95 μm regions, consistent with hydration, which likely post-dates atmospheric entry. The region of maximum reflectance is also shifted relative to the interior spectra: from ~0.58 to ~0.75 μm. The fusion crust spectra are suggestive of magnetite in terms of reflectance peak position and broad absorption band in the 1 μm region, consistent with observations that magnetite production accompanies atmospheric ablation (Blanchard and Cunningham, 1974), and could be spectrally dominant at low abundances (Cloutis et al., 2011b). Consequently the fusion crust spectra could have spectral contributions from pre-terrestrial magnetite and magnetite formed during passage through the atmosphere (Blanchard and Cunningham, 1974).

When various spectral metrics are applied to the data, it can be seen that there exists some overlap in terms of spectral slope (Fig. 3d), although the fusion crust spectra are generally brighter; however as noted, absolute reflectance, spectral slopes and depths of absorption bands of reflectance spectra of spots on a solid surface are sensitive to their texture (such as flatness, roughness, etc.). The most diagnostic parameter for fusion crust versus unaltered Murchison is the lack of a 0.7 μm region absorption band, the position of the reflectance peak (~0.75 μm), and a single absorption feature in the 1.00–1.05 μm interval, in the fusion crust spectra.

3.2. Intra-sample heterogeneity

As seen in Fig. 2, the Murchison hand samples exhibits obvious tonal variations, largely associated with varying concentrations of chondrules and calcium aluminum inclusions (CAIs). A number of regions of the Murchison slabs were extracted to produce ~0.5 g samples that were crushed and dry sieved to produce < 150 μm powders (labeled MSV*xxx* in Fig. 2). Their spectra are all broadly similar, with reflectance at 0.56 μm varying from 4.7% to 6.3% (Fig. 4a). The absolute differences in albedo between reflectance spectra of a single powder measured after emptying and refilling a sample cup (labeled MSV*xxxd*), one of which is shown in Fig. 4a, are < 1%. The spectra are all red-sloped, with similar 1.8/0.6 μm reflectance ratios: 1.31–1.38. They all show the expected Fe absorption band "triplet" (~0.75, 0.9, and 1.1 μm). Their band depths ranges are 3.5–5.3%, 2.5–4.3%, and 1.6–3.4%, respectively. They are generally positively correlated with each other, as they are all due to the same mechanism: abundance of Fe-bearing phyllosilicates. There are no systematic differences between samples derived from the interior versus those that included fusion crust. This is not unexpected, as fusion crust is thin (usually on the order of, at most, a few hundred μm (Thaisen and Taylor, 2009)) and readily diluted by the deeper material that was necessarily included in order to provide enough sample for the spectral measurements. However, the fusion crust is thick enough that it dominates reflectance spectra of intact fusion crust surfaces as shown in Fig. 3a versus Fig. 3c.

Straight line continuum-removed band center locations showed little variability: 0.74 μm, 0.90–0.93 μm, and 1.13 μm, with uncertainties on the order of ± 1 nm (Fig. 4b). In spite of attempts to sample the full range of visual differences across the slabs, the resulting spectra show no significant differences. This suggests that, at the ~0.5 g level, the samples are relatively homogeneous. Previously-measured laboratory spectra of Murchison (discussed in Cloutis et al., 2011b; Fig. 1) suggest that Murchison is more spectrally homogenous than we found, even when we compare spectra with minimal or no differences in grain size and observing conditions. This could be due to a number of causes, the most likely being that the use of < < 1 g quantities of sample would be less representative of the bulk (however we do not know the details of many of the previously-measured Murchison samples). Less likely, differences in sample preparation techniques between different

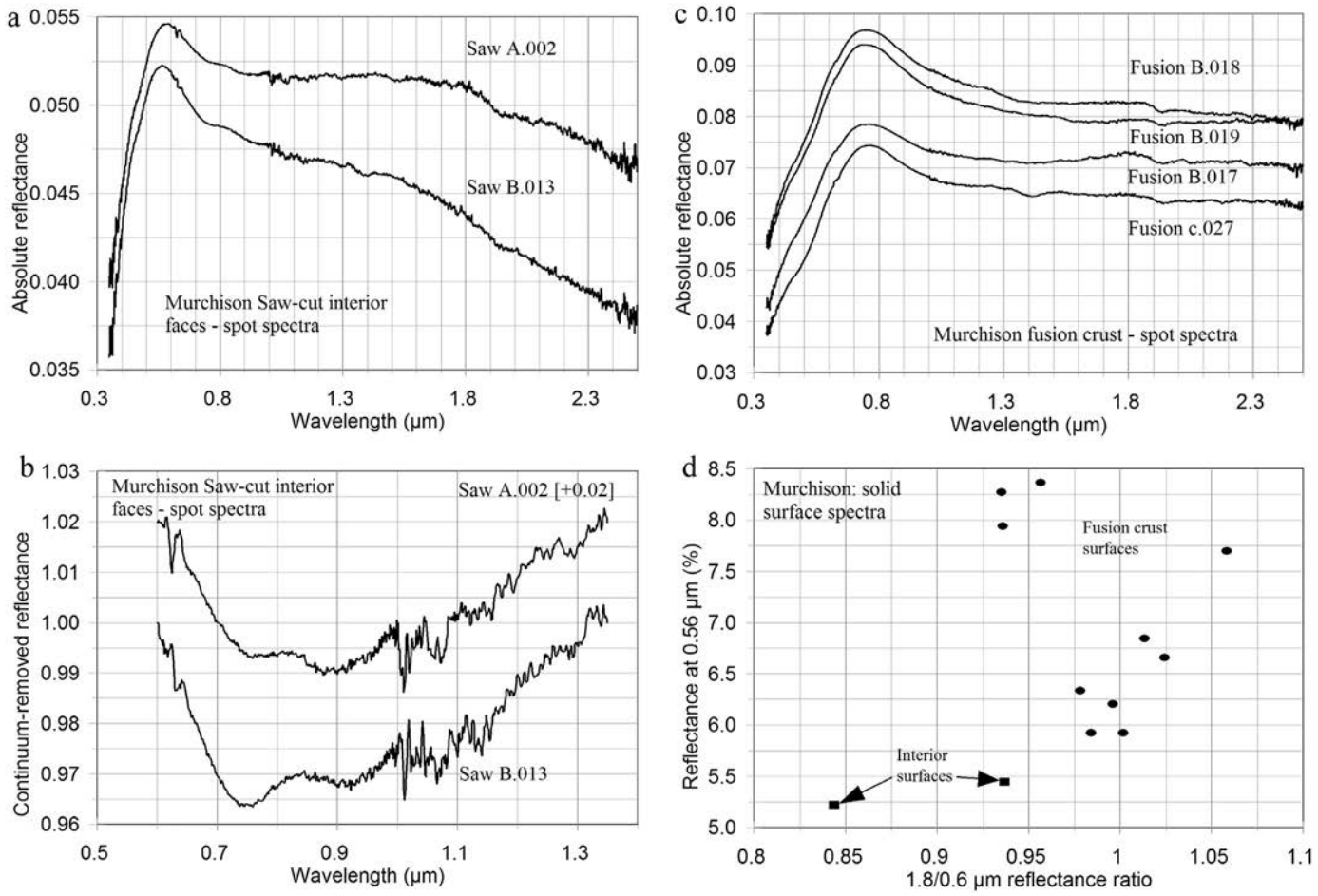

Fig. 3. ROM Murchison slab spectra. (a) Reflectance spectra of some of the saw-cut face spots. (b) Same spectra as (a) after removal of a straight line continuum from 0.6 to 1.35 μm. Number in brackets indicates linear vertical offset applied for clarity. (c) Reflectance spectra of some of the fusion crust spots. (d) 1.8/0.6 μm reflectance ratio versus reflectance at 0.56 μm; squares: interior surfaces; circles: fusion crust surfaces. < 90 μm powder spectra generally plot off the right side of the figure (1.8/0.6 μm reflectance ratios of 1.04–1.58 and reflectance at 0.56 μm of 3.2–6.1%). (For interpretation of the references to color in this figure, the reader is referred to the web version of this article)

investigators could cause some spectral differences, but these are likely to be restricted to albedo, slope, and perhaps band depths.

Intra-sample spectral heterogeneity is greater for different subsamples of Murchison measured by different investigators. For Murchison powders previously measured, with a minimum grain size of zero and maximum between 45 and 200 μm (Fig. 4c), it can be seen that not all of the spectra show a well-defined 0.7 μm region absorption feature, but otherwise all are red-sloped and exhibit a 1 μm region absorption feature. There is also no clear trend of reflectance as a function of grain size for these samples, suggesting that Murchison can be variable in terms of many potentially diagnostic spectral parameters. Fig. 4d shows the variability of two spectral metrics for powder spectra from the RELAB archive and previous investigators (Johnson and Fanale, 1973; Gaffey, 1974, 1976; Salisbury et al., 1975; Miyamoto et al., 1982, 2000; Calvin et al., 1999; Gillis-Davis et al., 2015; Matsuoka et al., 2015). While some of the variability is due to the relative sizes of the two data sets, it can be seen that variability across all Murchison samples is high: reflectance at 0.56 μm ranges from ~2.5% to 7%, and spectral slopes range from somewhat blue- to strongly red-sloped. There is a rough positive correlation between spectral slope and reflectance at 0.56 μm, but this may be due to the use of different subsamples and grain size ranges by different investigators. A positive correlation between albedo and spectral slope was seen by Johnson and Fanale (1973) for different sized powders of various CCs. In the case of the 0.9 μm absorption feature (Fig. 4e), all Murchison powder spectra exhibit an absorption feature in this region.

3.3. Grain size effects (1): decreasing maximum grain size

Reflectance spectra of the single ~1 g subsample of Murchison that was crushed and dry-sieved to progressively smaller maximum grain size is shown in Fig. 5a. With decreasing maximum grain size, the spectra become progressively more red-sloped and brighter, consistent with previous results (Johnson and Fanale, 1973). In all cases, the Fe absorption band triplet is apparent. The straight line continuum-removed spectra (Fig. 5b) show similarities to each other in terms of the shape and depth of the absorption features.

With decreasing maximum grain size, the following systematic spectral trends were found: (1) increase in visible region spectral slope (0.56/0.4 μm reflectance ratio increased from 1.32 to 1.47); (2) increase in overall slope (1.8/0.6 μm reflectance ratio increased from 1.32 to 1.47); (3) increase in reflectance at 0.56 μm (from 4.3% to 5.7%); and (4) a less systematic increase in 0.7 μm band depth (from 3.4% to 4.3%). The relationship between 1.8/0.6 μm reflectance ratio (a measure of spectral slope) and visible region reflectance (as measured at 0.56 μm) as a function of grain size is shown in Fig. 5c. It can be seen that decreasing maximum grain size leads to redder and brighter spectra. The scatter in the data is likely attributable to "natural" variability in duplicate

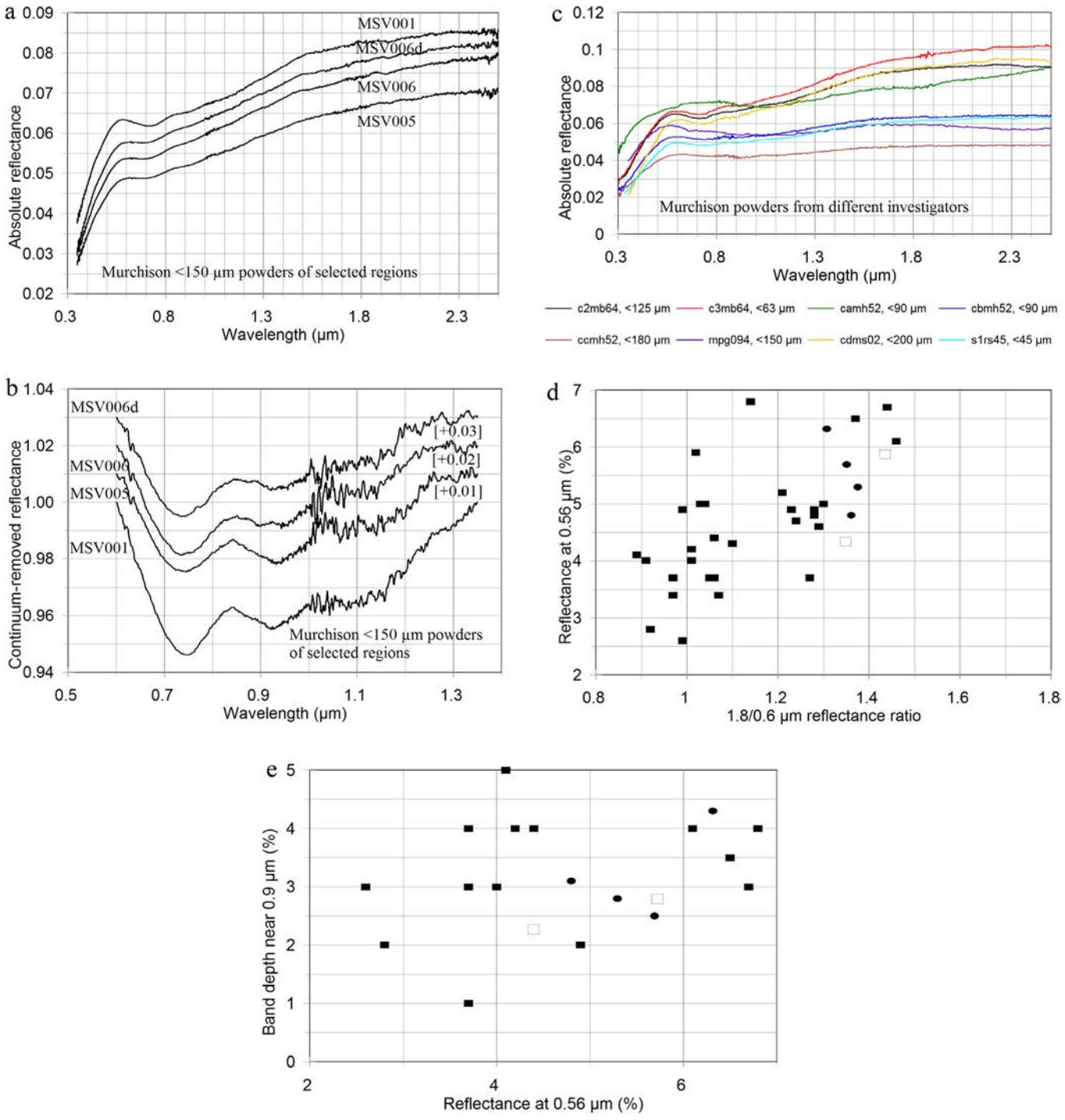

Fig. 4. Reflectance spectra of powdered (< 150 µm) ROM Murchison subsamples – see Fig. 2 for location of samples. (a) MSV001, MSV005, and two spectra of MSV006, with the second measured after emptying and repacking the sample. These show the differences that may arise due to repacking of a powdered sample. (b) Same spectra as (a) after removal of a straight line continuum from 0.6 to 1.35 µm. Number in brackets indicates linear vertical offset applied for clarity. (c) RELAB archive reflectance spectra of Murchison powders with a minimum grain size of ~0 µm. (d) 1.8/06 µm reflectance ratio versus reflectance at 0.56 µm for < 150 powder subsamples of Murchison measured in this study (filled circles), < 45 µm powders of Murchison measured in this study (dashed squares), and RELAB archive spectra of Murchison powdered samples of various grain sizes (filled squares). (e) Same as (d) for reflectance at 0.56 µm versus 0.9 µm region band depth. (For interpretation of the references to color in this figure, the reader is referred to the web version of this article).

reflectance spectra of the same sample (e.g., Cloutis et al., 2011b), which can be on the order of up to ± 0.5% absolute. This value is less than the full range of variability seen for the samples, suggesting that the trend is real but the values are subject to uncertainties.

The 0.9 and 1.1 µm bands did not show a systematic change in depth with grain size, but they are weaker and broader than the 0.7 µm band, and are more sensitive to the presence of other CM phases, such as magnetite. The 0.7, 0.9, and 1.1 µm absorption band centers showed no or small (< 30 nm) variations with changes in maximum grain size, with the greatest variability associated with

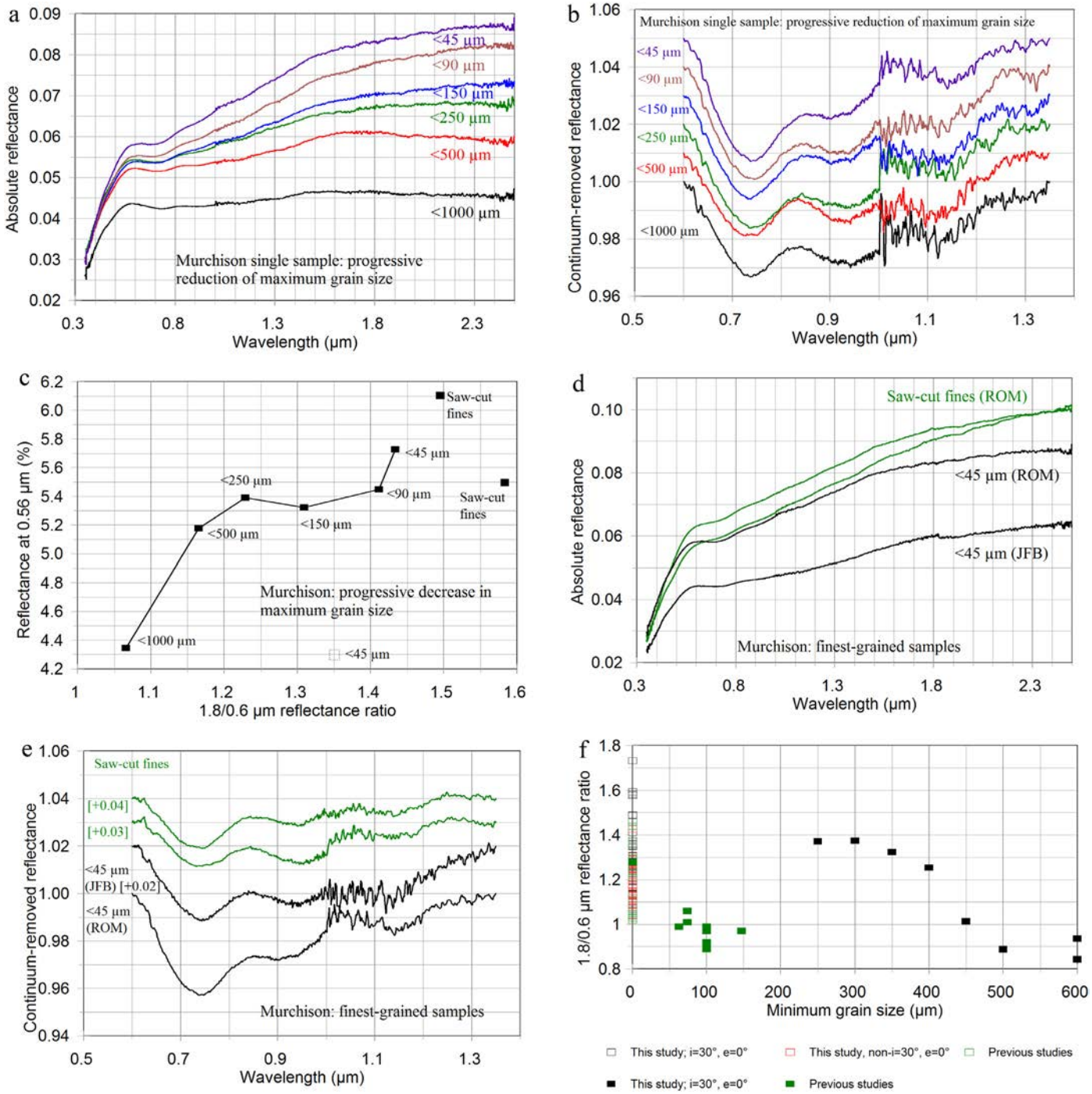

Fig. 5. Grain size effects on Murchison reflectance spectra. (a) The reflectance spectra of the single ROM Murchison subsample crushed to progressively smaller maximum grain size (see text for details). (b) Same spectra as (a) after removal of a straight line continuum from 0.6 to 1.35 μm. Each spectrum is offset by + 0.01 from the spectrum below it for clarity. (c) 1.8/0.6 μm reflectance ratio versus absolute reflectance at 0.56 μm of the spectra from (a). Also shown are data points for two saw-cut fines spectra from (d), and an additional < 45 μm spectrum (dashed rectangle: the < 45 μm sample used to produce the coarse + fines series of samples). Slab spectra (not shown) plot off the left side of the figure because they have blue-sloped spectra (i.e., 1.8/0.6 μm reflectance ratio of < 1). (d) Reflectance spectra of < 45 μm powders of two different subsamples of Murchison, and saw-cut fines (predominantly < 5 μm) acquired during preparation of the ROM Murchison subsample. (e) Same spectra as (d) after removal of a straight line continuum from 0.6 to 1.35 μm. Each spectrum is linearly vertically offset by the amount indicated in brackets for clarity. Minimum grain size (f), average grain size (g), and maximum grain size (h) versus 1.8/0.6 μm reflectance ratio of Murchison spectra. See legends for details. The filled squares are for the spectra from (a). For clarity, slabs are assigned a minimum grain size of 600 μm in (f), average grain size of 900 μm in (g), and maximum grain size of 1200 μm in (h). See legend for details (previous study data points with no viewing geometry information are for spectra measured at geometries other than $i = 30°$ and $e = 0°$). (i) Average grain size of the progressively crushed Murchison subsample versus band depth in the 0.7 (circles) and 0.9 μm (rectangles) regions. Data points for slab surfaces and saw-cut fines are as indicated on the figure, and the dashed symbols are for the < 45 μm sample used for the fine + coarse mixtures. (For interpretation of the references to color in this figure legend, the reader is referred to the web version of this article).

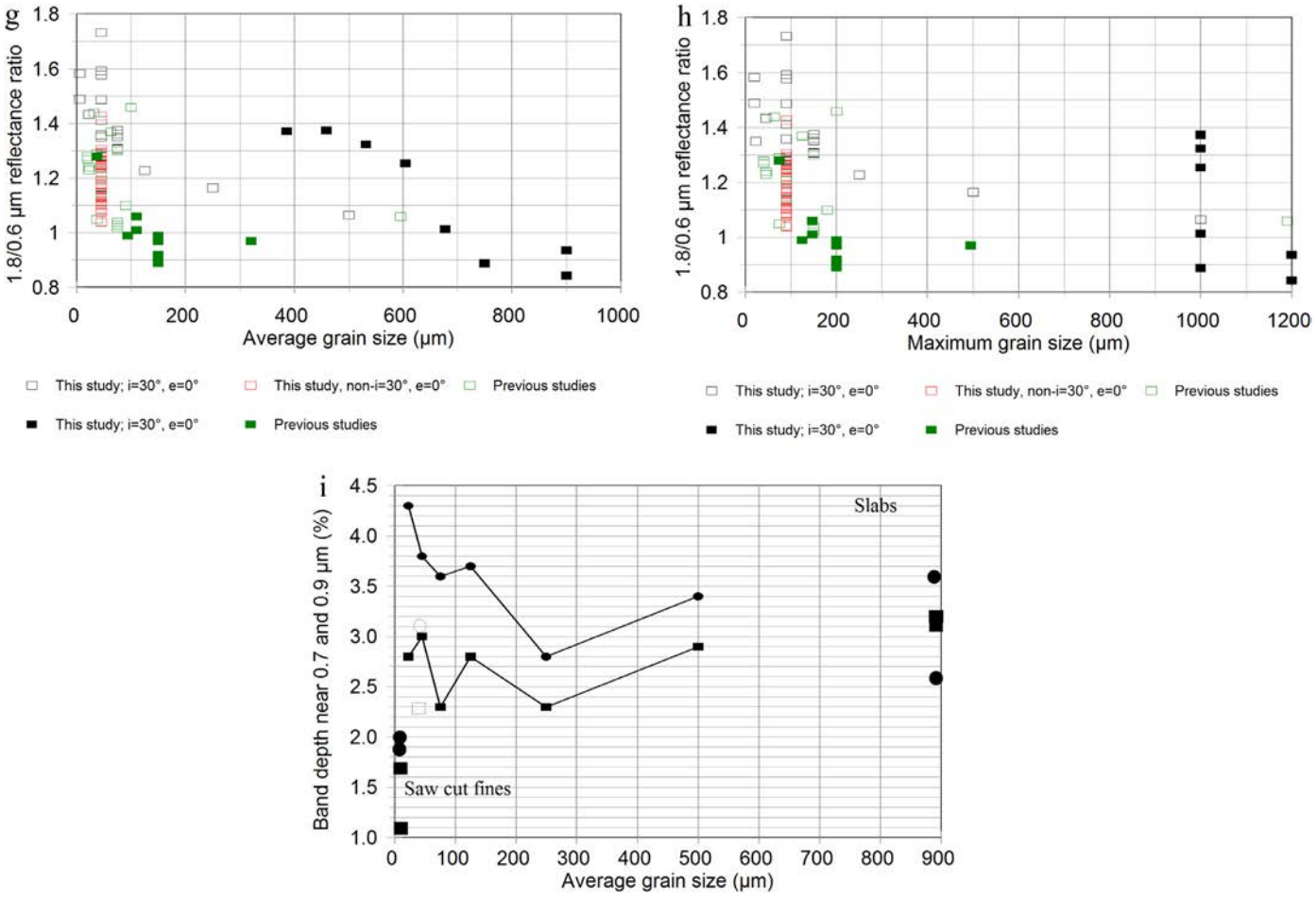

Fig. 5. Continued

the noisier 1.1 µm band, which we generally ignore in favor of the 0.7 and 0.9 µm region bands. The variations are of the same magnitude as was seen in some duplicate spectra of the same subsample (after emptying and repacking the sample).

Saw-cut fines saved during preparation of the ROM Murchison subsamples are finer-grained than the < 45 µm powders, with a maximum grain size of ~20 µm, and the vast majority of the grains being < 5 µm. These finest-grained samples continue the trend seen for progressive reduction in maximum grain size, being more red-sloped, generally brighter, and with shallower 0.7, 0.9, and 1.1 µm absorption bands than the < 45 µm powder spectra (Fig. 5c, d). The straight line continuum-removed spectra (Fig. 5e) show the reduction in depths of the Fe triplet set of bands, but they are still readily detectable, with depths on the order of 1–2%. XRD analysis of the saw-cut fines (e.g., Izawa et al., 2018) found trace amounts (likely < 1 wt%) of aluminum oxide as the only contaminant from the sample preparation process.

When the entire sample suite is considered, the greatest influence on spectral slope (1.8/0.6 µm reflectance ratio) appears to be minimum grain size (Fig. 5f) rather than average (Fig. 5g) or maximum (Fig. 5h) grain size. For the samples from this study measured at $i = 30°$ and $e = 0°$ we see a decrease in slope with increasing minimum grain size (black points in Fig. 5f). Reflectance at 0.56 µm is not able to distinguish samples on the basis of minimum, average, or maximum grain size. Band depths in the 0.7 and 0.9 µm region shows no consistent systematic trend (Fig. 5i). Saw-cut fines have band depths lower than any of the powders or slabs. Slab spectra band depths are variable but higher than saw-cut powder values.

Grain size effects on Murchison spectra include increased spectral slopes in the visible and infrared regions with decreasing particle size. Similar effects of particle size variations on spectral reflectance properties of meteorite, rock, and mineral powders have been widely reported (e.g., Adams and Filice, 1967; Gradie and Veverka, 1982; Capaccioni et al., 1990; Hiroi et al., 1994; Cooper and Mustard, 1999).

3.4. Grain size effects (2): increasing abundance of fine-grained particles

In addition to progressive crushing of a single Murchison subsample, we also investigated the spectrum-altering effects of progressive increases in the amount of a fine-grained (< 45 µm) fraction added to a 500–1000 µm powder using the "JFB" Murchison powder. The end member spectra are as expected: the 500–1000 µm powder is darker and more blue-sloped than the < 45 µm powder (Fig. 6a). With increasing < 45 µm fraction, the spectra approach that of the pure < 45 µm spectrum. With 10 wt% < 45 powder, the spectrum becomes nearly flat and by 20 wt.% < 45 µm powder, the spectrum is decidedly red-sloped, within ~10% of the 1.8/0.6 µm reflectance ratio value of the pure < 45 µm powder, and < 0.2% absolute difference of its reflectance at 0.56 µm (Fig. 6b). With increasing fines, the 0.7 µm band becomes shallower, as expected, approaching the value of the < 45 µm end member spectrum. The 0.9 and 1.1 µm bands also become shallower, with the greatest change seen with the initial addition of 10% fines

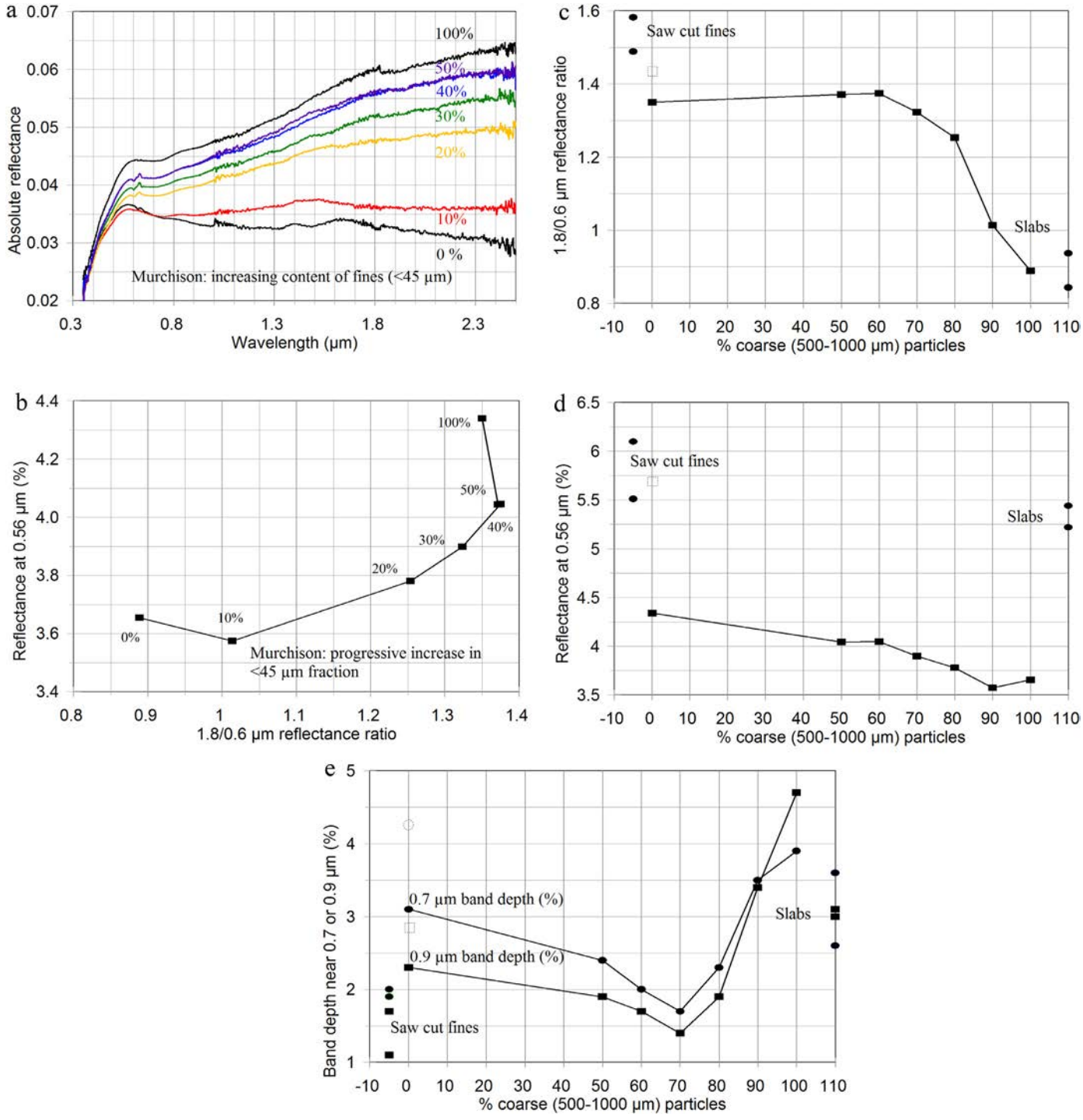

Fig. 6. Reflectance spectra of the JFB Murchison samples: varying proportions of fine-grained (< 45 μm) and coarse-grained (500–1000 μm) powders. (a) Reflectance spectra of each mixture. (b) 1.8/0.6 μm reflectance ratio versus reflectance at 0.56 μm as a function of wt% fine-grained powder. The saw-cut fine spectral parameters are not shown but plot well off the top left corner of this figure (1.8/0.6 μm reflectance ratio of 0.84–0.94, and 0.56 μm absolute reflectance of 5.2–5.4). Another < 45 μm spectrum plots off the top of the figure (reflectance at 0.56 μm: 5.7%; 1.8/0.6 μm reflectance ratio of 1.35 – this is for the < 45 μm sample made from progressive crushing of a Murchison subsample to pass through progressively finer sieves). (c) Percentage coarse particles (500–1000 μm) in the mixtures versus 1.8/0.6 μm reflectance ratio. Points for saw-cut fines and slabs are indicated by circles at −5 and 110 wt% respectively, for clarity. (d) Same as (c) for reflectance at 0.56 μm. (e) Same as (c) for band depths in the 0.7 (circles) and 0.9 μm (rectangles) regions. Data points for an additional < 45 μm spectrum (from the progressive crushing series) are indicated with a dashed rectangle in (c), and (d), and dashed rectangle (0.9 μm band depth) and dashed circle (0.7 μm band depth) in (e). Data points for saw-cut fines (assigned a % coarse value of −5 for clarity), and slabs (assigned a % coarse value of 110% for clarity) are also shown. (For interpretation of the references to color in this figure, the reader is referred to the web version of this article).

(*on-line supplement*). Powdered surfaces that may appear to be fine-grained could contain significant proportions of larger particles, and their spectral influence would be minimal compared to the (perhaps volumetrically minor) fines. The metrics for the coarse + fine mixtures show how ~60–70 wt% coarse particles are required to appreciable affect spectral slope, how slab spectra have similar slopes to coarse particles, and how saw-cut fines are appreciable redder than the < 45 μm powder (Fig. 6c). Reflectance at 0.56 μm (Fig. 6d) indicates that saw-cut fines are brighter than < 45 μm powders as expected, that slab spectra may also be brighter, although reflectance depends on surface texture, and that increasing fine fraction causes an increase in reflectance. Band depth in both the 0.7 and 0.9 μm regions show an initial decrease and then increase in band depth with increasing fraction of fine-grained particles (Fig. 6e); saw-cut fines have lower band depths than the < 45 μm fraction but comparable to the 50–80 wt% coarse particle mixtures, while slab spectra band depths are intermediate between the end members. The 0.7 and 0.9 μm region band depth data for the progressively crushed sample (Fig. 5i), by comparison, show no clear systematic trends – band depths are comparable to the 0 wt% and 80–90 wt% coarse particle spectra band depth.

3.5. Particle packing

We attempted to isolate the effects of microporosity (i.e., porosity between individual grains) by measuring reflectance spectra of the same < 90 μm powder as a regularly packed powder ("regular"), the sample surface fluffed with a needle ("fluffy"), tamped with the face of a glass slide ("dense"), and the densely-packed powder with a thin and thicker coating of airfall powder. The spectra were measured at $i = 30°/e = 0°$ and $i = 45°/e = 45°$. The spectra of the $i = 30°/e = 0°$ samples are shown in Fig. 7a. They all show the same overall behavior: evident 0.7–1.1 μm absorption bands, and an overall red slope. Reflectance is highest for the densely-packed sample and the densely-packed sample with a light coating of airfall dust, followed by the densely-packed sample with the heavier coating of airfall dust, the regularly packed sample, and finally the fluffy sample. Reflectance varies from 3.0% to 4.3% at 0.56 μm (a 43% relative variation).

The spectra of the same samples measured at $i = 45°/e = 45°$ (Fig. 7b) show the same consistent red slope and sequence of changes in absolute reflectance, with the fluffy sample spectrum showing the lowest overall reflectance. However, the range of albedos is higher, varying between 1.1% and 4.9% at 0.56 μm. These data suggest that viewing geometry will influence overall reflectance, in the sense that spectra acquired at higher phase angles could have a wider range of values due to differences in porosity, including lower lows and higher highs than reflectance spectra measured at lower phase angles. In all cases, spectral slope, as measured by the 1.8/0.6 μm reflectance ratio, is higher for the $i = 45°/e = 45°$ spectra as compared to the $i = 30°/e = 0°$ spectra (Fig. 7c, d); it also decreases with decreasing porosity for both sets of phase angle measurements. This is the well-known phase-reddening effect that is also seen in other meteorites and for asteroids (e.g., Cloutis et al., 2011a, 2011b; Sanchez et al., 2012; Ciarniello et al., 2017; Schröder et al., 2017).

The data also indicate that while absolute reflectance correlates with porosity, porosity has little effect on spectra slope for the spectra measured at $i = 30°/e = 0°$: 1.8/0.6 μm reflectance ratio varies from 1.25 to 1.28. However, for the $i = 45°/e = 45°$ spectra, the 1.8/0.6 μm reflectance ratio varies more widely and systematically: it is lowest for the densely-packed sample (1.36) and highest for the fluffy sample (1.73) with the other samples intermediate between these end members (*on-line supplement*).

The 'fluffy' samples consistently show larger 0.7 μm band depths than regular or 'packed' samples. These spectra and derived parameters demonstrate the complexity of the interaction between viewing geometry and aggregation state. Previous studies (e.g., Hapke et al., 1998; Kar et al., 2016) have found that changes in absolute reflectance are a function of both porosity and surface roughness. Kar et al. (2016) reflectance spectra show increasing reflectance (at 632.8 nm) with decreasing porosity for a number of geological materials, similar to our results.

3.6. Viewing geometry effects

We measured reflectance spectra of a regularly-packed < 90 μm powder of Murchison at multiple phase angles, including forward-scatter and back-scatter geometries, all in the principal plane, and all relative to our Spectralon standard measured at $i = 15°/e = 0°$. Spectral metrics are provided in the *on-line supplement*, and selected results are discussed below.

3.6.1. Fixed incidence angles

Reflectance spectra acquired at a fixed i of 0° (Fig. 8a), show an expected drop in overall reflectance with increasing e. Spectral slope varies slightly (1.04 to 1.17 for the 1.8/0.6 μm reflectance ratio) but the change is not systematic. With increasing e, the spectra appear more concave down and with the peak reflectance shifting to shorter wavelengths. The 0.7 μm band shows a slight increase in depth (from 2.2% to 2.6%), while the 0.9 and 1.1 μm band depths show non-systematic changes. The highest phase angle spectrum in this series ($i = 0°/e = 60°$) shows shifts in the position of the Fe triplet band set minima to longer wavelengths (by ~30–60 nm).

Reflectance spectra acquired at a fixed i of 15° (Fig. 8b) show variable spectral slopes ranging from overall red to slightly blue with a concave down profile, but all are red-sloped over the 0.6 to 1.8 μm interval. The characteristic absorption features in the 0.7–1.1 μm region are evident in all cases (when the vertical scale is reduced), with the 0.7 μm band being the deepest, ranging from 1.1–3.2% deep. Visible region albedo varies widely (from 1.3% to 5.2% at 0.56 μm). The highest albedo and reddest slope is seen in the smallest angle backscatter geometry ($i = 15°/e = -30°$ ($p = 15°$)), followed by the smallest near-normal geometry ($i = 15°/e = 0°$ ($p = 15°$)), and the second smallest backscatter geometry ($i = 15°/e = 45°$ ($p = 30°$)). The lowest reflectance and bluest spectral slopes are seen in the larger angle backscatter and forward scatter spectra ($i = 15°/e = -60°$ ($p = 45°$)), ($i = 15°/e = 60°$ ($p = 75°$)).

When the incidence angle is increased to 30° (Fig. 8c), the spectra can be more red-sloped than the $i = 15°$ spectra (1.8/0.6 μm reflectance ratio up to 1.27 versus a maximum of 1.22 for the $i = 15°$ spectra, and 1.17 for the $i = 0°$ spectra). The range of visible albedos is somewhat less, and the 0.7–1.1 μm absorption feature is still evident but generally shallower. As with the $i = 15°$ spectra, the highest albedos are seen in the forward scatter spectra and lowest phase angles, while the larger phase angle spectra are darkest and most blue-sloped.

When the incidence angle is further increased to 45° (Fig. 8d), the spectra continue to exhibit red 0.6–1.8 μm slopes, some being overall concave down, as well as the 0.7–1.1 μm region absorption features. As before, the spectra acquired with backscattering geometry have the highest overall reflectance, which decreases from the highest emission angle (60°) to lowest emission angle (15°) in backscatter, and hence from lowest phase angle (15°) to highest phase angle (30°). As before, the highest phase angle spectra in forward scatter mode have the lowest overall reflectance. Continuing the trend seen with increasing i, the range of reflectance at 0.56 μm is further decreased (1.5–4.0%).

Finally, when i is increased to 60° (Fig. 8e), we see a further decrease in the range of albedo (1.1–2.4% at 0.56 μm), including a decrease in the lowest values. The backscatter geometry measurements have, as before, the generally highest albedos, and

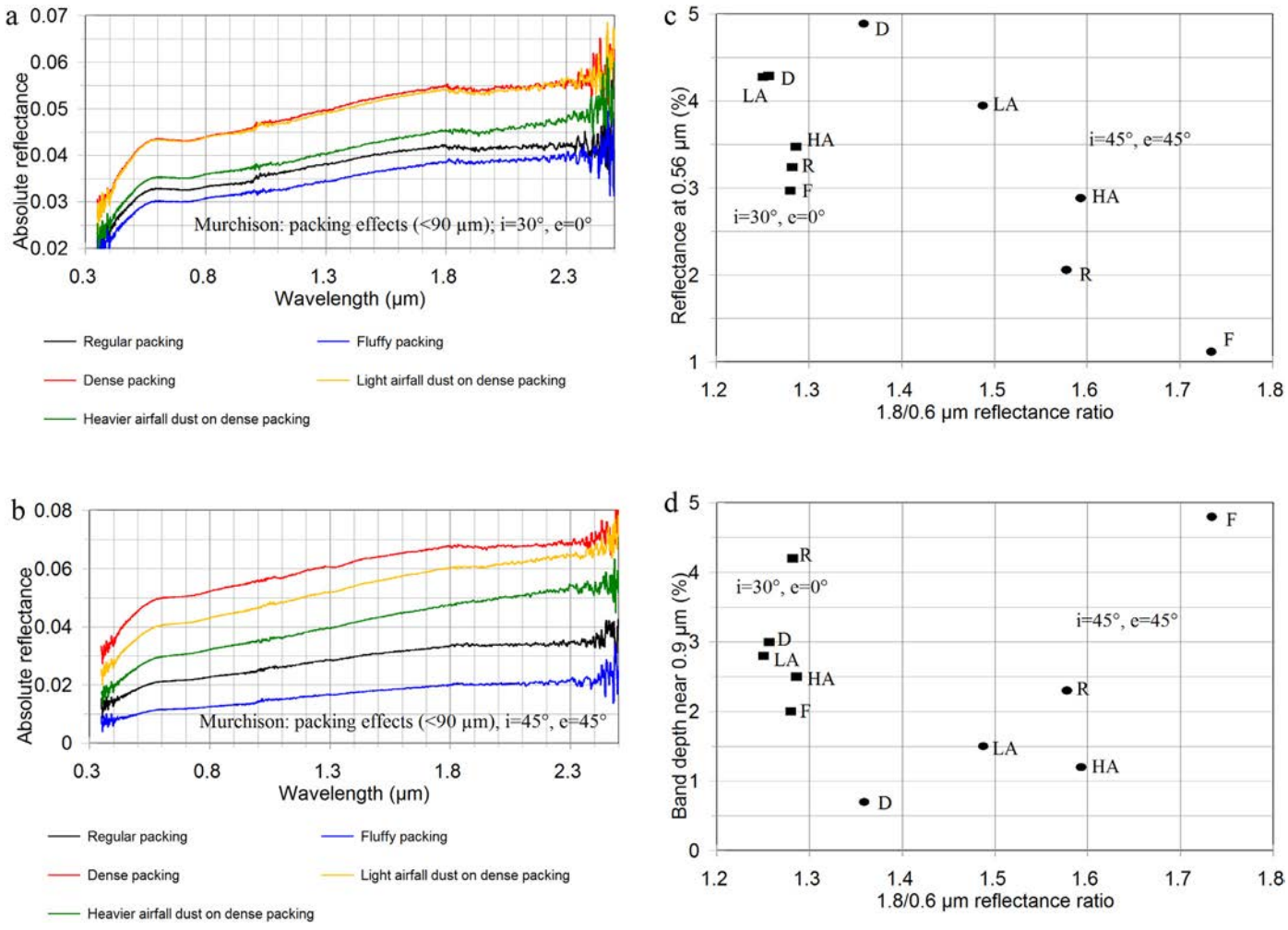

Fig. 7. Reflectance spectra of $a < 90\,\mu m$ fraction of the JFB Murchison powders as a function of particle packing. (a) Spectra acquired at $i = 30°$ and $e = 0°$ (b) Spectra acquired at $i = 45°$ and $e = 45°$ (b) 1.8/0.6 μm reflectance ratio versus reflectance at 0.56 μm; squares: $i = 30°$, $e = 0°$ spectra; circles: $i = 45°$, $e = 45°$. R: regular packed, F: fluffy; D: dense pack; LA: light airfall; HA: heavy airfall. See text for definition of these terms. (d) Same as (c) versus band depth in the 0.9 μm region. (For interpretation of the references to color in this figure, the reader is referred to the web version of this article).

which again decreases from the highest to the lowest emission angle in backscatter (the $i = 15°/e = 60°$spectrum shows evidence of some incident light entering the pick-up fiber, which can be an issue with high phase angle measurement using our current configuration). The 0.7–1.1 μm absorption features are still present in the spectra, but generally of reduced depth relative to the lower incidence angle spectra.

3.6.2. Fixed emission angles

When we examine the spectra on the basis of a single emission angle, many of the same trends seen with a single incidence angle are present. When e is fixed at 0° (Fig. 9a), albedo decreases with increasing i, as expected (from 4.4% to 1.1% at 0.56 μm) and the spectra become slightly less red sloped, while the 0.7–1.1 μm region absorption bands remain apparent.

Reflectance spectra acquired at a fixed e of 15° (Fig. 9b) are all red-sloped, and the characteristic absorption features in the 0.7–1.1 μm region are evident. Visible region albedo varies from ~1.1% to 4.3% at 0.56 μm. The two highest-albedo spectra are those measured at the smallest phase angle (15°), and albedo decreases with increasing phase angle, for both the forward and backscatter geometries. For identical phase angles, those acquired in backscatter geometry have higher albedo than those acquired in forward scatter geometry. The 0.7 μm band depth appears to be largely insensitive to i for $e = 15°$, ranging from 2.9% to 3.2%. The 1.8/0.6 μm reflectance ratio increases slightly with increasing phase angle.

When e is increased to 30°(Fig. 9c), the spectra are generally less red sloped, while the range of visible albedos is largely unchanged (and highest for the lowest phase angle spectra). As with the $e = 15°$ spectra, the highest albedos are seen in the backscatter and lowest phase angle spectra, while the larger phase angle spectra are darkest. The 0.7–1.1 μm absorption bands are still evident, being deepest for the smallest phase angle spectra.

When the emission angle is further increased to 45° (Fig. 9d), the spectra become less red-sloped and more concave-down, and the 0.7–1.1 μm absorption features become less distinct in many of the spectra, with 0.7 μm band depths < 1% in the highest phase angle spectra. As before, the spectra acquired in backscattering geometry and lowest phase angle have the highest overall reflectance, while the highest phase angle spectra are the darkest. Continuing the trend seen with increasing e, the range of reflectance at 0.56 μm is further reduced (1.2–4.9%).

Finally, when e is increased to 60° (Fig. 9e), we see a further decrease in the range of albedo, including a decrease in the lower limit. The backscatter geometry measurements have, as before, the generally highest albedos, although the specular $i = e = 60°$ spectrum is present in the higher albedo group. The 0.7–1.1 μm absorption features are still present in the spectra, but reduced in depth, many being < 1% deep.

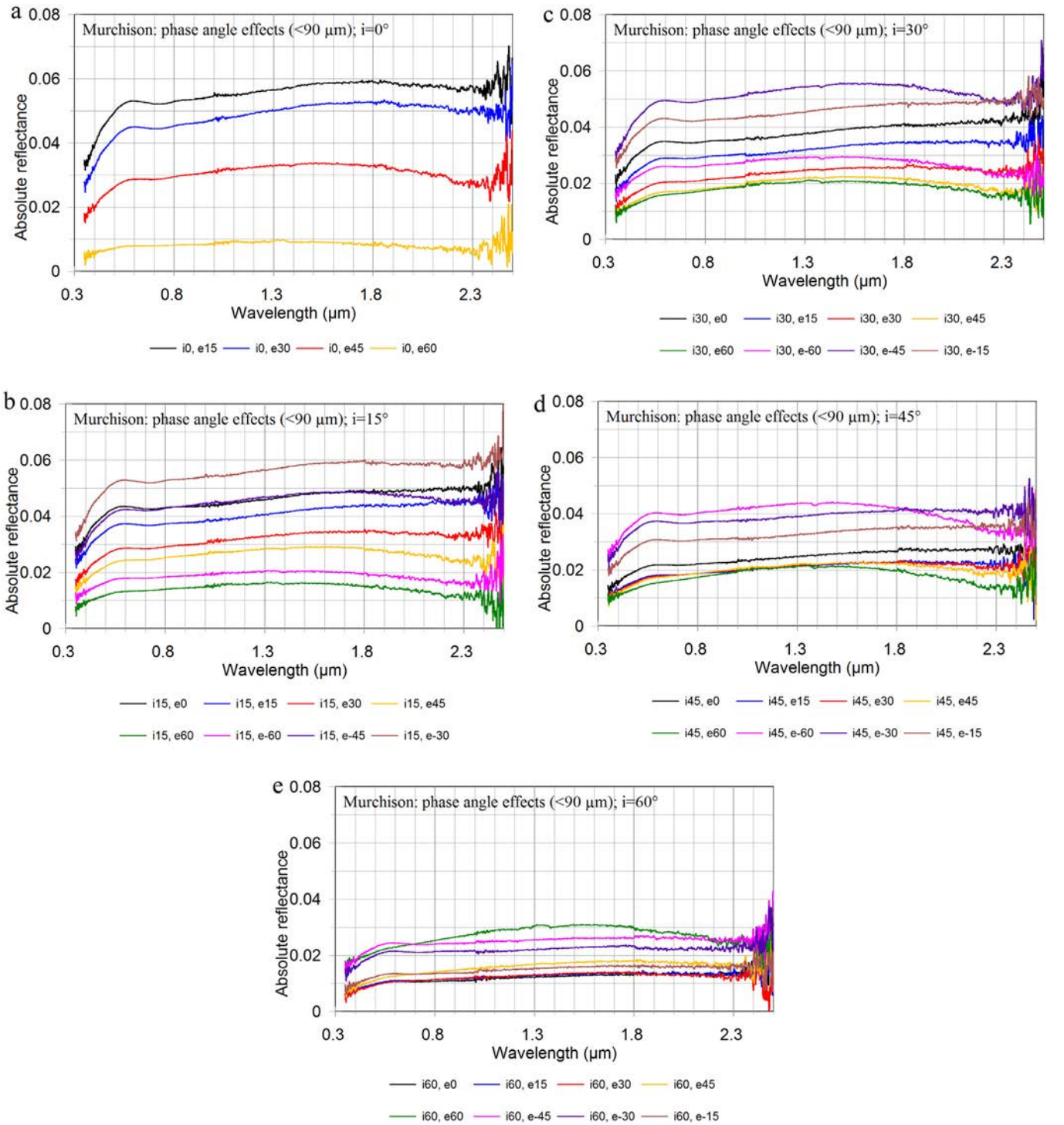

Fig. 8. Reflectance spectra of $a < 90\,\mu m$ fraction of the JFB Murchison powder as a function of incidence angle (i). (a) $i = 0°$. (b) $i = 15°$. (c) $i = 30°$. (d) $i = 45°$. (e) $i = 60°$. (For interpretation of the references to color in this figure, the reader is referred to the web version of this article).

3.6.3. Fixed phase angles

Reflectance spectra acquired at a fixed phase angle (p) of 15° (Fig. 10a), show variable spectral slopes, all being red over the 0.6–1.8 μm range but some being blue-sloped beyond 1.8 μm, and showing generally evident 0.7–1.1 μm absorption bands. Albedos are all > 2.4% at 0.56 μm. As with the results for a constant i or e, the spectra acquired in backscatter mode and close to normal incidence have the highest reflectance. The 0.7–1.1 μm Fe triplet absorption band set is evident in all the spectra, with 0.7 μm band depth ranging from 2.2% to 5.3%.

Reflectance spectra acquired at a fixed p of 30° (Fig. 10b) also show variable spectral slopes, all being red over the 0.6–1.8 μm interval, but some having an overall concave-down profile. The characteristic absorption features in the 0.7–1.1 μm region are evident in all cases. The range of visible region albedo is shifted downward from the $p = 15°$ values (1.7–4.6% at 0.56 μm versus

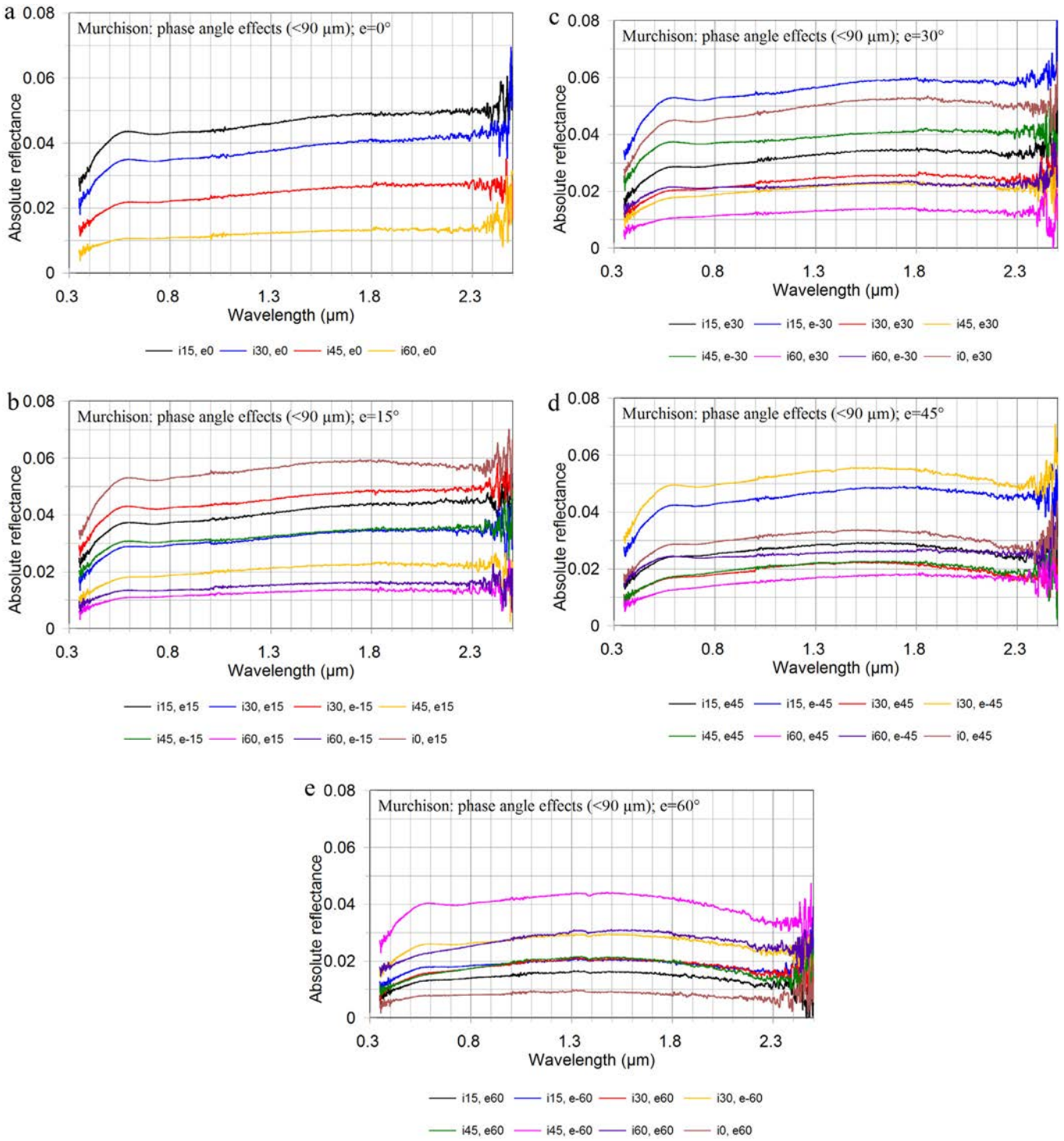

Fig. 9. Reflectance spectra of $a < 90\,\mu m$ fraction of the JFB Murchison powder as a function of emission angle (e). (a) $e = 0°$. (b) $e = 15°$. (c) $e = 30°$. (d) $e = 45°$. (e) $e = 60°$. (For interpretation of the references to color in this figure, the reader is referred to the web version of this article).

2.2–5.3% for $p = 15°$). The highest albedos are seen in the spectra acquired in backscatter mode and closest to near-normal geometry.

When the phase angle is further increased to 45° (Fig. 10c), the spectra continue to exhibit red slopes and more concave-down shapes at higher emission angles, and the range of albedos continues to decrease (ranging from 1.1% to 2.8% at 0.56 μm). There are less systematic trends in the data, although the spectra with i or e of 60° are the darkest. The 0.7–1.1 μm region absorption bands are generally more subdued than the lower phase angle spectra.

For the spectra acquired with $p = 60°$ (Fig. 10d), we see a further decrease in the range of albedo, including a decrease in the lowest value. Spectral slopes are red or overall concave-down. The measurements with i or $e < 60°$ are the brightest. The 0.7–1.1 μm absorption features are still detectable in the spectra but subdued: 0.7 μm band depths are all < 1%.

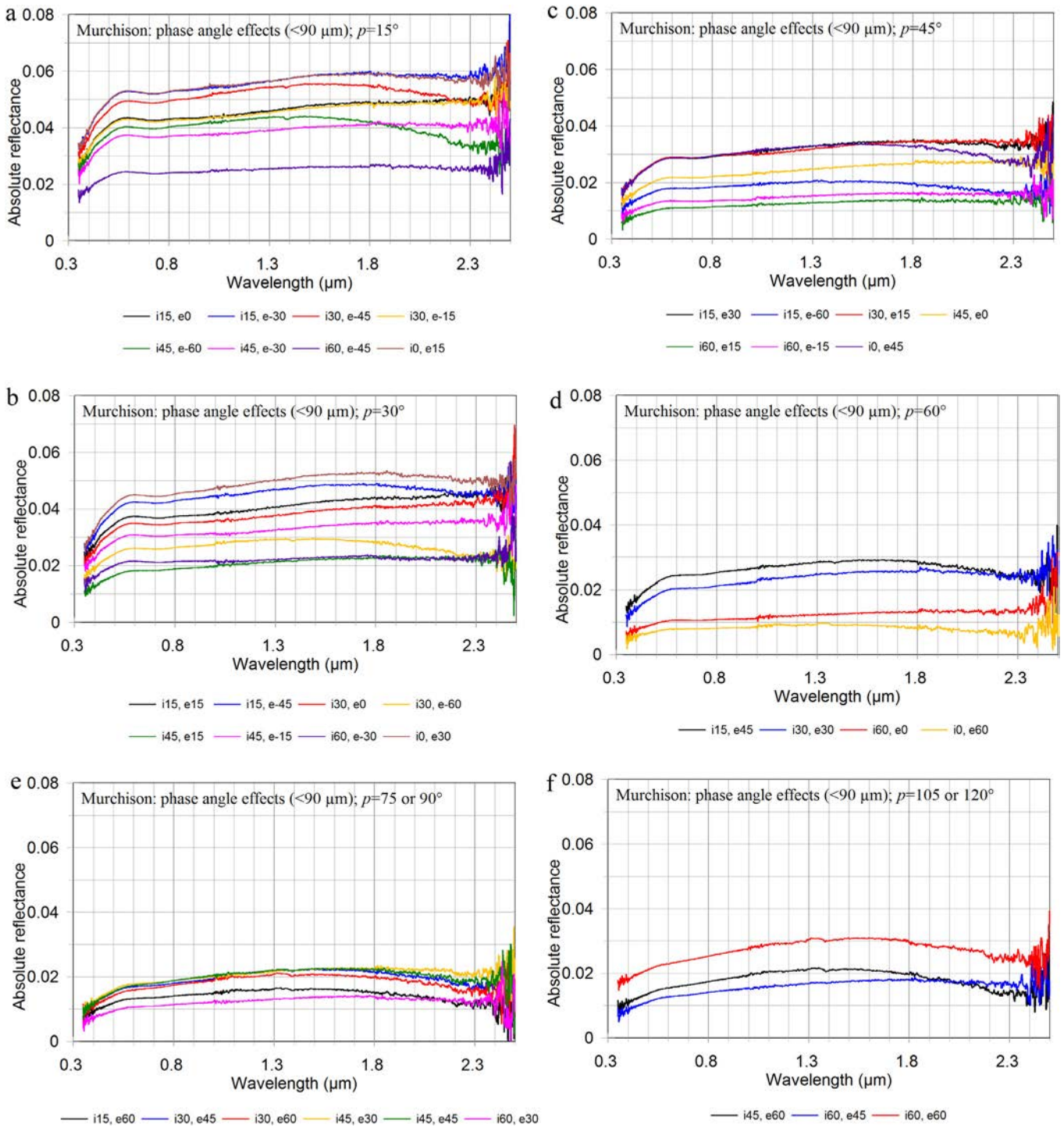

Fig. 10. Reflectance spectra of $a < 90\,\mu m$ fraction of the JFB Murchison powder as a function of phase angle (p). (a) $p = 15°$. (b) $p = 30°$. (c) $p = 45°$. (d) $p = 60°$. (e) $p = 75$ or 90°. (f) $p = 105$ or 120°. (For interpretation of the references to color in this figure, the reader is referred to the web version of this article).

The trend of decreasing albedo with increasing phase angle continues for spectra acquired at $p = 75$ or 90° (Fig. 10e). Most of the spectra are concave-down over the 0.6–2.5 μm range, and 0.7–1.1 μm region absorption bands are subdued, many being < 1% deep (ranging from 0.2% to 2.2% deep). As before, the brightest spectra are those for which i or e is < 60°.

At the highest phase angles, $p = 105°$ or 120° (Fig. 10f), the spectra are decidedly concave down over the 0.6–2.5 μm range and reflectance is low. The brightest spectrum is for the specular geometry ($i = e = 60°$). The 0.7–1.1 μm region absorption bands are very subdued (< 1% deep).

3.6.4. Viewing geometry effects summary

When various spectral metrics are examined for all the phase angle data, certain general trends emerge. For spectra acquired in backscattering geometry (Fig. 11a), there is a general decrease in spectral slope (1.8/0.6 μm reflectance ratio) with increasing reflectance. Points that fall off the trend are associated with the highest emission angles ($i = 60°$). The forward scatter geometry spectra are generally flatter and show no obvious correlation between spectral slope and reflectance at 0.56 μm. There is a weak positive correlation of band depth in the 0.9 μm region as a function of reflectance at 0.56 μm (Fig. 11b). The points that fall

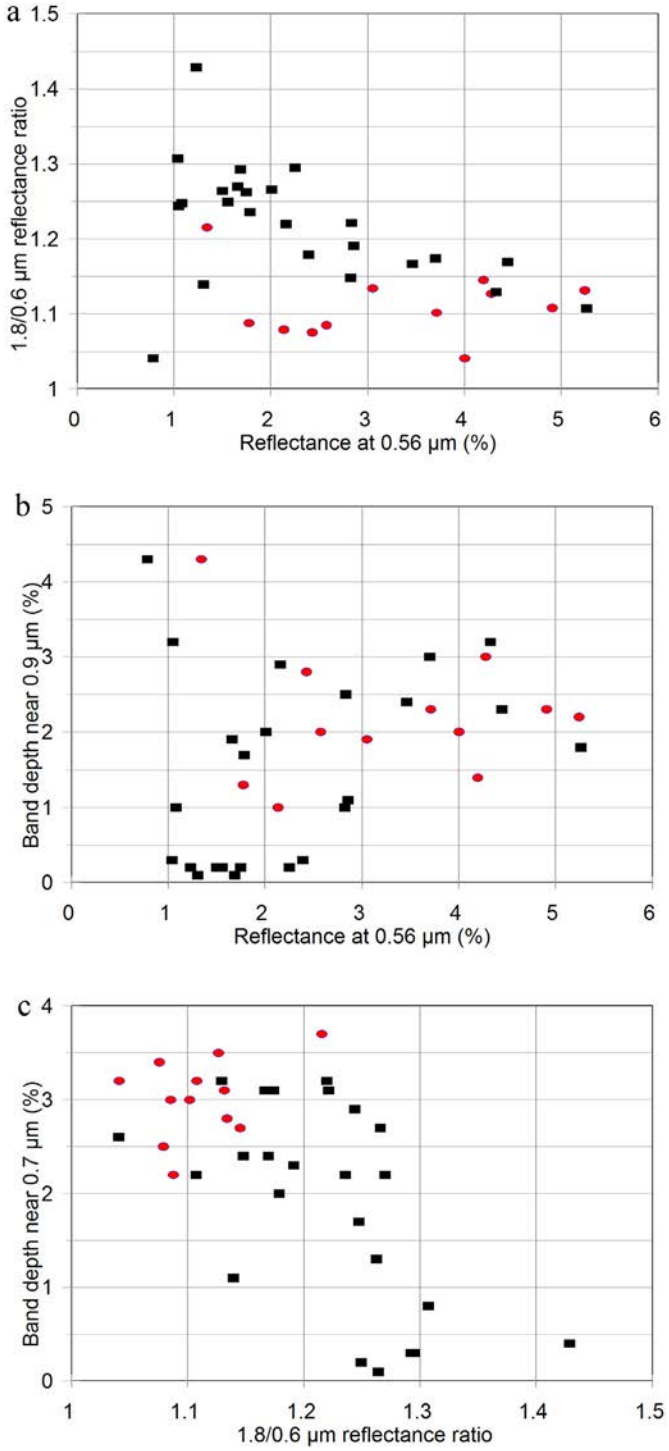

Fig. 11. Various spectral metrics as a function of viewing geometry. (a) Reflectance at 0.56 µm versus 1.8/0.6 µm reflectance ratio. (b) Reflectance at 0.56 µm versus 0.9 µm region absorption band depth. (c) 1.8/0.6 µm reflectance ratio versus 0.7 µm region absorption band depth. Black squares: forward scatter geometry; red circles: backscatter geometry. (For interpretation of the references to color in this figure, the reader is referred to the web version of this article).

of the general trend are mostly those associated with the highest incidence angle ($i = 60°$). There is no obvious correlation between the 1.8/0.6 µm reflectance ratio and 0.9 µm region absorption band depth, but a negative correlation appears for the 0.7 µm absorption band depth for the forward scatter geometry data (Fig. 11c).

The qualitative phase angle observations discussed above are shown in Fig. 12a–c. It can be seen that the 1.8/06 µm reflectance ratio generally reddens with increasing emission angle up to between 30° and 60° emission angle, and decreases toward the highest emission angle (Fig. 12a). The backscatter measurements are generally the least red-sloped.

Reflectance at 0.56 µm shows less systematic trends (Fig. 12b). In the forward scattering regime ($e > 0°$), the decrease in reflectance with increasing e becomes flatter with increasing i, and at $i = 60°$, this decrease is no longer present. In the backscattering regime ($e < 0°$), the point at which reflectance at 0.56 µm decreases with increasingly negative e moves to more negative values with increasing i.

Band depth data also show general but not rigorously systematic variations as a function of incidence angle. The depth of the 0.7 µm region absorption band (Fig. 12c) decreases with increasing emission angle in the forward scattering regime, with the magnitude of the decrease becoming larger with increasing incidence angle. Band depth is fairly constant at $e = 0°$regardless of i. In the backscattering regime (i.e., negative e), band depth seems to decrease the most at lower incidence angles, but the magnitude of the change is less than for the forward scattering spectra. Trends are less apparent for the depth of the 0.9 µm region absorption band (Fig. 12d). The highest emission angle spectra again show the largest decrease in band depth with increasing emission angle, but the lower incidence angle spectra show significant scatter. There is also a higher degree of scatter in the backscatter regime data for $i = 60°$ data, but the other incidence angle series show a progressively smaller decrease in band depth with increasing e. The relationship between absorption band depths and viewing geometry is complex. Both increases and decrease can be observed for a single sample (e.g., Gradie et al., 1980), and this behavior is likely a function of composition and sample type. The trends we observe for Murchison indicate that, overall, band depths decrease with increasing phase angle (Fig. 12c and d), but there are often exceptions, such as the increase in band depth in backscatter geometry for the $i = 45°$ spectra.

The general reddening that is observed with increasing emission angle and phase angle has also been observed for other CCs (Beck et al., 2012) and other types of meteorites/asteroids (e.g., Cloutis et al., 2011a, 2011b; Sanchez et al., 2012; Ciarniello et al., 2017; Schröder et al., 2017). Decreases in reflectance with increasing phase angle for many geological materials have been observed by a number of researchers (e.g., Gradie et al., 1980; Capaccioni et al., 1990).

4. Discussion

The various parameters, physical and observational, that have been isolated in this study allow us to discern trends and identify any unique spectral metrics that can relate to these parameters. While Murchison is only one of many CM2 chondrites, our results are generally applicable to CM2 chondrites, as they share many common spectral characteristics (Cloutis et al., 2011b), and are likely also applicable to other CC groups that are characterized by low reflectance and subdued absorption features.

Some level of spectral diversity is seen within the CM group (Cloutis et al., 2011b). As a group, reflectance spectra of CM powders range from blue to red, likely due to compositional differences. It has also been found that brighter spectra are also generally more red-sloped (Cloutis et al., 2011b). Absolute reflectance also varies, which also is likely related to compositional differences among CMs. The most ubiquitous spectral property of CM chondrites is the presence of three absorption bands near 0.7, 0.9, and 1.1 µm, whose depths vary largely in tandem (because they are associated with Fe-bearing serpentine) and generally

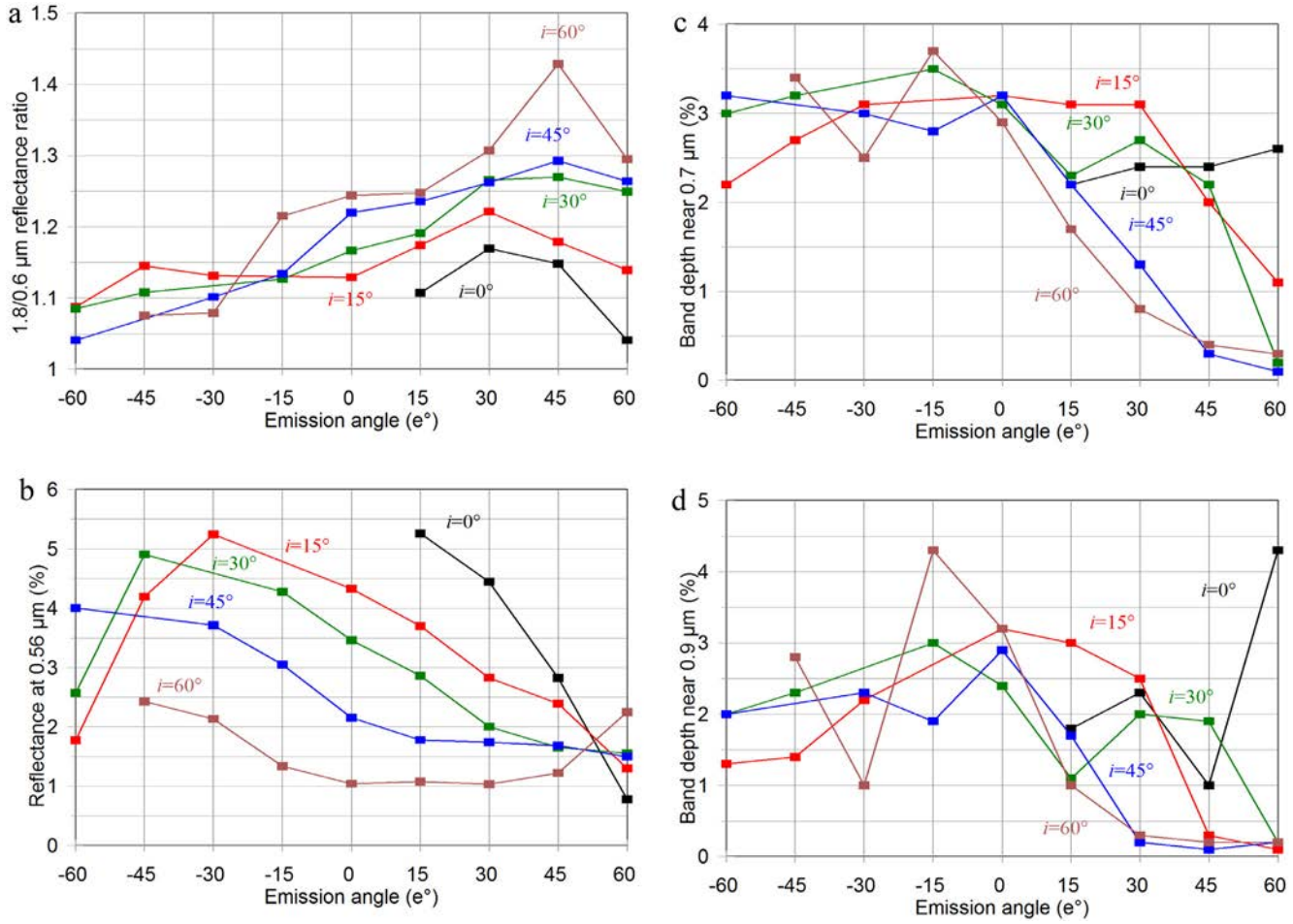

Fig. 12. Spectral metrics as a function of emission angle for the different incidence angle series of measurements. (a) *e* versus 1.8/06 µm reflectance ratio. (b) *e* versus reflectance at 0.56 µm. (c) *e* versus depth of the 0.7 µm region absorption band. (d) *e* versus depth of the 0.9 µm region absorption band. (For interpretation of the references to color in this figure, the reader is referred to the web version of this article).

increase with increasing aqueous alteration. This absorption band triplet is the most distinguishing feature of CM2 chondrites; as mentioned, similar, but weaker, features are present in spectra of some CI1 chondrites (Cloutis et al., 2011a) and thermally metamorphosed CM-like chondrites (Cloutis et al., 2012b). This absorption feature is also a distinguishing characteristic of the Cgh/Ch asteroid taxonomic groups (Bus and Binzel, 2002; DeMeo et al., 2009).

Because the results of this study and derived spectral variations as a function of the parameters we examined are strictly only relevant to our samples of Murchison, they are best utilized in a qualitative rather than quantitative manner. In other words, spectral trends rather than absolute values are more reliable for constraining what compositional, physical or observational parameters are varying. The observed variations in spectral metrics from this study are summarized in Table 2.

From this table it can be seen that the various parameters we examined, and their effects on reflectance spectral metrics, are sometime unique, but not always. In addition, we have not included the fact that CM chondrites show variability in all spectral metrics (absorption band depths, absorption band positions, slopes, and albedo) (Cloutis et al., 2011b), suggesting that assigning spectral differences to physical and observational properties rather than compositional differences may not be possible. However, constraining the cause of spectral variations across the surface of a single asteroid (rather than between different asteroids) may be more tractable, particularly if spectral variations are combined with geomorphological analysis.

We can examine the results in Table 2 in two ways: their relationship to the different factors examined in this study, or as ensembles of possibly unique combinations. Here we look at the different combinations of spectral metrics that show correlations with some physical or observational parameter.

1. *Increasing absolute reflectance at 0.56 µm (no other trends):* this trend is most associated with a decrease in porosity for spectra measured at $i = 30°$ and $e = 0°$.

2. *Decrease in band depths at 0.7 and/or 0.9 µm (no other trends):* this is most associated with porous dust overlying a more compacted layer, and seems to be independent of viewing geometry ($i = 30°/e = 0°$, and $i = 45°/e = 45°$).

3. *Bluer slopes (decreasing 1.8/0.6 µm reflectance ratio) AND decreasing absolute reflectance at 0.56 µm (no other trends):* this paired trend is most associated with grain size, specifically with slabs as compared to powders, increasing maximum grain size for a powder, and a decreasing abundance of fine-grained (< 45 µm) material.

4. *Redder slopes (increasing 1.8/0.6 µm reflectance ratio) AND decreasing absolute reflectance at 0.56 µm (no other trends):* this paired trend is most associated, and seen most clearly, with increasing incidence angle for low emission angles ($e = 0°$ and 15°).

Table 2
Spectral trends of Murchison spectra measured in this study.

Parameter	Band depths[a]	Band positions[a]	Reflectance ratios 1.8/0.6 and 0.56/0.40 μm	Absolute reflectance[b]	Other/notes
Slab versus powder[c]	No clear trends	No differences	Bluer (decrease)	Same or darker	
Intra-sample splits	No differences	No differences	No difference	No differences	Differences on the order of duplicate spectra
Decreasing maximum grain size	Slight increase	No trend	Redder (increase)	Increase	
Increasing fine-grained component	Decrease	No trend	Redder (increase)	Increase	
Decreasing porosity ($i=30°$, $e=0°$)	No change or trend	No change	No change/trend	Increase	See text for details
Decreasing porosity ($i=45°$, $e=45°$)	Increase	No change	Bluer (decrease)	Increase	See text for details
Thicker airfall dust[c] ($i=30°$, $e=0°$)	Decrease	No change	No change/trend	No change or trend	See text for details
Thicker airfall dust[d] ($i=45°$, $e=45°$)	Decrease	No change	No trend	No trend	See text for details
Increasing $e°$[e] (all $i°$)	Decrease	No change	General increase	Decrease[f]	
Increasing $i°$					
$e=0°$ or 15°	No trend	No change	Redder (increase)	Decrease[g]	
$e=30°$	General decrease	Possible increase	Redder (increase)	Decrease	
$e=45°$	General decrease	Possible decrease	Redder (increase)[h]	Decrease[h]	
$e=60°$	General decrease	Possible decrease	Redder (increase)	General increase[h]	
Increasing $p°$[i]	Decrease[j]	No trend	No trend	Decrease[j]	
Increasing $p°$[k]	Decrease[j]	No trend	General increase	Decrease	

Symbols: $i°$ = incidence angle; $e°$ = emission angle; $p°$ = phase angle.
[a] Refers to depths of absorption bands in the 0.7 and/or 0.9 μm regions. The 1.1 μm band shows similar behavior to the 0.9 μm band, but was not rigorously quantified.
[b] Refers to absolute reflectance at 0.56 μm.
[c] Relative to regularly packed <45 μm powder measured at i=30° and e=0°.
[d] Relative to regularly packed <45 μm powder measured at i=45° and e=45°.
[e] Same trends seen when $i°$ and $e°$ are on the same side of the surface normal (i.e., backscatter geometry).
[f] Increases for i=60° when $i°$ and $e°$ are on opposite sides of the surface normal (i.e., forward scatter geometry).
[g] Increase for e=15° when $i°$ and $e°$ are on the same side of the surface normal (i.e., backscatter geometry).
[h] Trends not apparent when $i°$ and $e°$ are on the same side of the surface normal (i.e., backscatter geometry).
[i] $e°$ and $i°$ are on the same side of the surface normal (i.e., backscatter geometry).
[j] No discernible trend below p=45°; decrease most evident for p>45°.
[k] $e°$ and $i°$ are on opposite sides of the surface normal (i.e., forward scatter geometry).

5. *Decreasing band depths at 0.7 and/or 0.9 μm AND decreasing absolute reflectance at 0.56 μm (no other trends):* this pairing was most evident for increasing phase angle when $p > 45°$.

6. *Increasing band depths at 0.7 and/or 0.9 μm AND bluer slopes (decreasing 1.8/0.6 μm reflectance ratio) AND increasing absolute reflectance at 0.56 μm:* the simultaneous change in these three trends is associated with decreasing porosity at high phase angle ($i=45°/e=45°$), as well as when emission angle or phase angle is decreasing (with the exception of $i=60°$ and $p > 60°$).

7. *Decreasing band depths at 0.7 and/or 0.9 μm AND possibly increasing 0.7 and/or 0.9 μm band position(s) AND redder slope (increasing 1.8/0.6 μm reflectance ratio) AND changing reflectance at 0.56 μm:* simultaneous change in all four of these spectral metrics is associated with increasing incidence angle when $e \geq 30°$. In all cases, increasing incidence angle leads to the same kinds of changes in band depths, band positions, and slope. However, it should be noted that the changes in band position are not entirely systematic and are usually on the order of 10–20 nm. The trends in slope and reflectance are not apparent for $e=45°$ in backscatter geometry, and the trend in slope is not apparent for $e=60°$ in backscatter geometry. Absolute reflectance decreases with increasing i for $e=0°$, 15°, 30°, or 45°, but increases with increasing i for $e=60°$.

We found that the positions of the 0.7, 0.9, and 1.1 μm absorption bands are the most invariant features; they do not show systematic variations except a possible increase with increasing $i°$ for $e \geq \sim 30°$ A previous study (Cloutis et al., 2011b) of CM spectra measured at $i=30°$ and $e=0°$, found no variations in band positions as a function of composition or petrologic grade. Thus, for observational data where a range of phase angles are available (for a single target), any observed changes in band positions would likely be attributable to viewing geometry effects, specifically changes in emission angle.

This study investigated phase angle effects in some detail. If phase angle can be independently determined, it would be possible to reduce ambiguities in the potential causes of variations in spectral metrics seen on a potential CM parent body.

The band depth parameters investigated here appear to be less sensitive to non-compositional effects than spectral slopes; however, some important variations do occur. For example, at some viewing geometries, especially those with large phase angles, band depths can vary dramatically. Even though viewing geometry and local topography can be accounted for during data processing, local topography (at a scale below that derivable from a shape model or topographic variations at the sub-pixel scale), could affect a single pixel reflectance spectrum. The fact that sub-pixel (or local) topography can affect reflectance spectra has long been known (see Pilorget et al., 2016 for an excellent discussion of this topic). Apparent spectrally-derived compositional variations which show strong correlations with topography should be interpreted with caution, particularly if highly variable or extreme topography is observed or suspected.

Non-compositional effects can produce spectral changes that are similar to those due to intra-sample variability. An analysis combining slope and absorption band parameters minimizes the ambiguities while interpreting the spectra. But given the unknown surface composition along with the observational limits and also the geometry/physical effects, removing ambiguities while analyzing and interpreting the spectra is likely impractical.

Our data also suggest that spectral variations within a single CC exist (in this case Murchison) that are due to compositional heterogeneities, are on the order of hundreds of milligrams. This is comparable to scales of heterogeneity seen in CMs and other CCs (e.g., Fuchs et al., 1973; Bischoff et al., 2006; Morlok et al., 2006; Herd et al., 2011; Jenniskens et al., 2012). However, on an asteroid surface we expect regolith gardening to rapidly obscure such fine-scale heterogeneities (e.g., Shestopalov et al., 2013).

The effectiveness of such processes will depend on many factors however, such as size of the body, its location, age, and geological history and conditions.

5. CM chondrites and asteroids

There are a number of scenarios that we envision for how spectroscopic variations derived from this study could be applied to analysis of observational data of possible CM parent bodies. For example, comparison of the spectra of different possible CM parent bodies (most likely present in the Cgh/Ch taxonomic group; Bus and Binzel, 2002; DeMeo et al., 2009) or the older Tholen (1984) G class (Burbine, 1998), could allow factors such as relative ages to be constrained, if a relationship exists between surface age and regolith physical properties, such as grain size (Vernazza et al., 2016).

A spectral metrics approach could be applicable to comparison of, for example, different terrains on a single CC parent body, where spatially resolved spectroscopic data are available (e.g., spectroscopic data from the Dawn, OSIRIS-REx and Hayabusa 2 missions). Such an approach could allow compositional differences to be discriminated from physical properties such as grain size. This also has implications for determining the sampleability of target areas on asteroids for sample return missions.

Many tens of asteroids have been tentatively proposed as parent bodies for CM2 chondrites (Burbine, 1998; Cloutis et al., 2011b, and references therein; Vernazza et al., 2016). A previous review of these associations (Cloutis et al., 2011b) found that possible parent bodies fell into a number of Tholen (1984) taxonomic classes, including B, BU, C, CG, CX, D, F, FC, G, M, P, S, and ST. The asteroid spectra were examined in terms of whether they exhibited the most ubiquitous diagnostic spectral feature: absorption features in the 0.7, 0.9, and 1.1 μm regions, as well as a less specifically diagnostic Fe^{3+} spin-forbidden absorption band in the 0.4 μm region. It was found that ∼95% of the considered asteroid spectra exhibited one or both of the 0.7 and 0.9 μm region absorption features (as compiled in Cloutis et al., 2011b). The largely diagnostic nature of these absorption features is strong evidence for a linkage of these asteroids to CM2 chondrites.

Asteroid taxonomic classifiers based on spectral shapes and absorption features are available for the ∼0.4–0.95 μm region (Bus and Binzel, 2002) and 0.45–2.45 μm interval (DeMeo et al., 2009). In both classification schemes, the Ch and Cgh classes are distinguished by a 0.7 μm region absorption feature, and hence most akin to CM chondrites. Our laboratory spectra show large variations in the depths of these absorption bands, but they appear to be very persistent. Previous research has also shown that the 0.7 μm feature can disappear with modest increases in temperature (Hiroi et al., 1993) that could arise from parent body metamorphism or close passage by the Sun.

The asteroid classification schemes of Bus and Binzel (2002) and DeMeo et al. (2009) use principal components analysis for taxonomic classification. While it is difficult to relate principal components to changes in specific spectral features, DeMeo et al. (2009) noted that the first few principal components relate mostly to differences in slope and presence/absence of 1 and 2 μm region absorption bands. They also noted that identification of Ch/Cgh class asteroids is best done visually, by examining whether a spectrum exhibits a 0.7 μm region absorption band, as such identifications are not captured well by principal components analysis.

6. Summary and conclusions

Viewing geometry, porosity, and grain size variations for a single CM2 chondrite can cause variations in a variety of spectral metrics, including absorption band depths, slopes, and absolute reflectance. The direction of changes and number of systematic spectral changes seen is often uniquely associated with changes in a particular variable. The 0.7, 0.9, and 1.1 μm absorption bands, which characterize CM2 chondrites, remain detectable, although can become nearly indistinguishable in some cases, particularly for high phase angle measurements. Our results also indicate that the relationship between absorption band depths and phase angle is not straightforward and depends on incidence and emission angles as well as whether the spectra are acquired in forward- or back-scatter geometry. The results of this study suggest that the causes of spectral variations that may be seen in disk-resolved (or rotationally resolved) spectra of possible CM2 parent bodies can be uniquely assigned to one mechanism. The relationships that have been found between changes in various spectral metrics and physical properties may help to determine sampleability of terrains on CM2 parent bodies.

The findings from this study include:

- Reflectance spectra of slabs are more blue-sloped and generally darker than powder spectra.
- Decreasing grain size leads to brighter and redder spectra, and a decrease in absorption band depths.
- The spectral properties of powdered samples are most affected by minimum grain size.
- Increasing thickness of fine-grained dust leads to a decrease in absorption band depths.
- Decreasing porosity of powdered samples leads to spectral changes that are a function of viewing geometry.
- Increasing phase angle leads to a decrease in reflectance and absorption band depths.
- Changes in viewing geometry (incidence, emission, phase angle), and whether spectra are acquired in forward or backscatter geometry all have measurable effects on reflectance, spectral slope, and absorption band depths.
- The diagnostic 0.7, 0.9, and 1.1 μm region absorption bands are remarkably persistent regardless of changes in viewing geometry and physical properties of the sample.
- On asteroids, apparent compositional variations that show strong correlations with topography, or that are acquired at high phase angles should be interpreted with caution.

Acknowledgments

The University of Winnipeg's HOSERLab was established with funding from the Canada Foundation for Innovation, the Manitoba Research Innovations Fund and the Canadian Space Agency, whose support is gratefully acknowledged. This study was supported by research grants from NSERC, the Canadian Space Agency, the Hatch foundation, and the University of Winnipeg. Thanks to Ian Nicklin, and Brendt Hyde at the Royal Ontario Museum for providing the Murchison sample at the heart of this study. Support for this work was also provided by the Remote, In Situ, and Synchrotron Studies for Science and Exploration (RIS^4E) node of NASA's Solar System Exploration Research Virtual Institute.

References

Adams, J.B., Filice, A.L., 1967. Spectral reflectance 0.4 to 2.0 microns of silicate rock powders. J. Geophys. Res. 72, 5705–5715.

Ammannito, E., De Sanctis, M.C., Ciarnello, M., Frigeri, A., Carrozzo, F.G., Combe, J.-P., Ehlmann, B.L., Marchi, S., McSween, H.Y., Raponi, A., Toplis, M.J., Tosi, F., Castillo-Rogez, J.C., Capaccioni, F., Capria, M.T., Fonte, S., Giardino, M., Jaumann, R., Longobardo, A., Joy, S.P., Magni, G., McCord, T.B., McFadden, L.A., Palomba, E.,

Pieters, C.M., Polanskey, C.A., Rayman, M.D., Raymond, C.A., Schenk, P.M., Zambon, F., Russell, C.T., 2016. Distribution of phyllosilicates on the surface of Ceres. Science 353. doi:10.1126/science.aaf4279.
Beck, P., Pommerol, A., Thomas, N., Schmitt, B., Moynier, F., Barrat, J.-A., 2012. Photometry of meteorites. Icarus 218, 364–377.
Binzel, R.P., Lupishko, D.F., Di Martino, M., Whiteley, R.J., Hahn, G.J., 2002. Physical properties of near-Earth objects. In: Bottke, Jr., W.F., Cellino, A., Paolicchi, P., Binzel, R.P. (Eds.), Asteroids III.. University of Arizona Press, Tucson, pp. 255–271.
Binzel, R.P., Rivkin, A.S., Stuart, J.S., Harris, A.W., Bus, S.J., Burbine, T.H., 2004. Observed spectral properties of near-Earth objects: results for population distribution, source regions, and space weathering processes. Icarus 170, 259–294.
Binzel, R.P., DeMeo, F.E., Burt, B.J., Cloutis, E.A., Rozitis, B., Burbine, T.H., Campins, H., Clark, B.E., Emery, J.P., Hergenrother, C.W., Howell, E.S., Lauretta, D.S., Nolan, M.C., Mansfield, M., Pietrasz, V., Polishook, D., Scheeres, D.J., 2015. Spectral slope variations for OSIRIS-REx target asteroid (101955) Bennu: possible evidence for a fine-grained equatorial bulge. Icarus 256, 22–29.
Bischoff, A., Scott, E.R.D., Metzler, K., Goodrich, C.A., McSween, H.Y., 2006. Nature and origins of meteoritic breccias. In: Lauretta, D.S. (Ed.), Meteorites and the Early Solar System II. University of Arizona Press, Tucson, pp. 679–712.
Blanchard, M.B., Cunningham, G.G., 1974. Artificial meteor ablation studies: olivine. J. Geophys. Res. 79, 3973–3980.
Bland, P.A., Cressy, G., Menzies, O.N., 2004. Modal mineralogy of carbonaceous chondrites by X-ray diffraction and Mössbauer spectroscopy. Meteorit. Planet. Sci. 39, 3–16.
Bland, P.A., Berry, F.J., Cadogan, J.M., Howard, K.T., Cressey, G., 2008. Fe-bearing mineral abundance in primitive chondrites by Mössbauer spectroscopy. Meteorit. Planet. Sci. 43, A25 (abstract).
Brearley, A.J., Jones, R.H., 1998. Chondritic meteorites. In: Papike, J.J. (Ed.), Planetary Materials. Mineralogical Society of America, Washington, D.C, p. 398.
Buchanan, P.C., Zolensky, M.E., Reid, A.M., 1993. Carbonaceous chondrite clasts in the howardites Bholghati and EEt87513. Meteoritics 28, 659–682.
Burbine, T.H., 1998. Could G-class asteroids be the parent bodies of the CM chondrites. Meteorit. Planet. Sci. 33, 253–258.
Burbine, T.H., 2014. Asteroids: planets, asteroids, comets and the solar system. In: Davis, A.M. (Ed.). In: Treatise on Geochemistry, 2. Elsevier, pp. 365–415.
Bus, S.J., Binzel, R.P., 2002. Phase II of the small main-belt asteroid spectroscopic survey. A feature-based taxonomy. Icarus 158, 146–177.
Calvin, W.M., Hamilton, V.E., King, T.V.V., 1999. Infrared observations of carbonaceous chondrites: petrologic diversity expressed in reflectance and emittance. Lunar Planet. Sci. 30 abstract #1495.
Capaccioni, F., Cerroni, P., Barucci, M.A., Fulchignoni, M., 1990. Phase curves of meteorites and terrestrial rocks: laboratory measurements and applications to asteroids. Icarus 83, 325–348.
Chapman, C.R., Salisbury, J.W., 1973. Comparison of meteorite and asteroid spectral reflectivities. Icarus 19, 507–522.
Ciarniello, M., De Sanctis, M.C., Ammannito, E., Raponi, A., Longobardo, A., Palomba, E., Carrozzo, F.G., Tosi, F., Li, J.-Y., Schröder, S.E., Zambon, F., Frigeri, A., Fonte, S., Giardino, M., Pieters, C.M., Raymond, C.A., Russell, C.T., 2017. Spectrophotometric properties of dwarf planet Ceres from the VIR spectrometer on board the Dawn mission. Astron. Astrophys. 598, A130.
Clark, R.N., Roush, T.L., 1984. Reflectance spectroscopy: quantitative analysis techniques for remote sensing applications. J. Geophys. Res. 89, 6329–6340.
Clark, R.N., King, T.V.V., Klewja, M., Swayze, G.A., Vergo, N., 1990. High spectral resolution reflectance spectroscopy of minerals. J. Geophys. Res. 95, 12653–12680.
Clark, B.E., Binzel, R.P., Howell, E.S., Cloutis, E.A., Ockert-Bell, M., Christensen, P., Barucci, M.A., DeMeo, F., Lauretta, D.S., Connolly, Jr.H., Soderberg, A., Hergenrother, C., Lim, L., Emery, J., Mueller, M., 2011. Asteroid (101955) 1999 RQ36: spectroscopy from 0.4 to 2.4 µm and meteorite analogs. Icarus 216, 462–475.
Cloutis, E.A., Hiroi, T., Gaffey, M.J., Alexander, C.M.O.D., Mann, P., 2011a. Spectral reflectance properties of carbonaceous chondrites: 1. CI chondrites. Icarus 212, 180–209.
Cloutis, E.A., Hudon, P., Hiroi, T., Gaffey, M.J., Mann, P., 2011b. Spectral reflectance properties of carbonaceous chondrites: 2. CM chondrites. Icarus 216, 309–346.
Cloutis, E.A., Hudon, P., Hiroi, T., Gaffey, M.J., 2012a. Spectral reflectance properties of carbonaceous chondrites: 3. CR chondrites. Icarus 217, 389–407.
Cloutis, E.A., Hudon, P., Hiroi, T., Gaffey, M.J., 2012b. Spectral reflectance properties of carbonaceous chondrites 4: aqueously altered and thermally metamorphosed meteorites. Icarus 220, 586–617.
Cloutis, E.A., Hudon, P., Hiroi, T., Gaffey, M.J., Mann, P., 2012c. Spectral reflectance properties of carbonaceous chondrites: 8. "Other" carbonaceous chondrites: CH, ungrouped, polymict, xenolithic inclusions, and R chondrites. Icarus 221, 984–1001.
Cooper, C.D., Mustard, J.F., 1999. Effects of very fine particle size on reflectance spectra of smectite and palagonitic soil. Icarus 142, 570–577.
de Leuw, S., Rubin, A.E., Schmitt, A.K., Wasson, J.T., 2009. Mn-Cr systematics for the CM2.1 chondrites QUE 93005 and ALH 83100: implications for the timing of aqueous alteration. Lunar Planet. Sci. 40 abstract #1794.
DeMeo, F.E., Carry, B., 2013. The taxonomic distribution of asteroids from multi-filter all-sky photometric surveys. Icarus 226, 723–741.
DeMeo, F.E., Binzel, R.P., Slivan, S.M., Bus, S.J., 2009. An extension of the Bus asteroid taxonomy into the near-infrared. Icarus 202, 160–180.
De Sanctis, M.C., Ammannito, E., Raponi, A., Marchi, S., McCord, T.B., McSween, H.Y., Capaccioni, F., Capria, M.T., Carrozzo, F.G., Ciarniello, M., Longobardo, A., Tosi, F., Fonte, S., Formisano, M., Frigeri, A., Giardino, M., Magni, G., Palomba, E., Turrini, D., Zambon, F., Combe, J.-P., Feldman, W., Jaumann, R., McFadden, L.A., Pieters, C.M., Prettyman, T., Toplis, M., Raymond, C.A., Russell, C.T., 2015. Ammoniated phyllosilicates with a likely Solar System origin on (1) Ceres. Nature 528, 241–244.
Fornasier, S., Lantz, C., Barucci, M.A., Lazzarin, M., 2014. Aqueous alteration on main belt primitive asteroids: results from visible spectroscopy. Icarus 233, 163–178.
Fuchs, L.H., Olsen, E., Jensen, K.J., 1973. Mineralogy, mineral-chemistry, and composition of the Murchison (C2) meteorite. Smithson. Contrib. Earth Sci. 10, 1–39.
Gaffey, M.J., 1974. A Systematic Study of the Spectral Reflectivity Characteristics of the Meteorite Classes with Applications to the Interpretation of Asteroid Spectra for Mineralogical and Petrological Information. Massachusetts Institute of Technology, Cambridge, MA Ph.D. Dissertation.
Gaffey, M.J., 1976. Spectral reflectance characteristics of the meteorite classes. J. Geophys. Res. 81, 905–920.
Gillis-Davis, J.J., Gasda, P.J., Bradley, J.P., Ishii, H.A., Bussey, D.B.J., 2015. Laser space weathering of Allende (CV2) and Murchison (CM2) carbonaceous chondrites. Lunar Planet. Sci. 46 abstract #1607.
Gounelle, M., Zolensky, M.E., Liou, J.C., Bland, P.A., Alard, O., 2003. Mineralogy of carbonaceous chondritic microclasts in howardites: identification of C2 fossil micrometeorites. Geochim. Cosmochim. Acta 67, 507–527.
Gradie, J., Veverka, J., 1982. The wavelength dependence of phase coefficients. Icarus 66, 455–467.
Gradie, J., Veverka, J., Buratti, B., 1980. The effects of scattering geometry on the spectrophotometric properties of powdered material. In: Proceedings of the 11th Lunar and Planetary Science Conference, pp. 799–815.
Grady, M.M., Graham, A.L., Barber, D.J., Aylmer, D., Kurat, G, Ntaflos, T., Ott, U., Palme, H., Spettel, B., 1987. Yamato-82042: an unusual carbonaceous chondrite with CM affinities. In: Proceedings of the 11th Symposium on Antarctic Meteorites, 46, pp. 162–178. Memoirs of NIP Special Issue.
Hanowski, N.P., Brearley, A.J., 2000. Iron-rich aureoles in the CM carbonaceous chondrites Murray, Murchison, and Allan Hills 81002: evidence for in situ aqueous alteration. Meteorit. Planet. Sci. 35, 1291–1308.
Hapke, B., Nelson, R., Smythe, W., 1998. The opposition effect of the moon: coherent backscatter and shadow hiding. Icarus 133, 89–97.
Harloff, J., Arnold, G., 2001. Near-infrared reflectance spectroscopy of bulk analog materials for planetary crust. Planet. Space Sci. 49, 191–211.
Herd, C.D.K., Blinova, A., Simkus, D.N., Huang, Y., Tarozo, R., Alexander, C.M.O'D., Gyngard, F., Nittler, L.R., Cody, G.D., Fogel, M.L., Kebukawa, Y., Kilcoyne, A.L.D., Hilts, R.W., Slater, G.F., Glavin, D.P., Dworkin, J.P., Callahan, M.P., Elsila, J.E., De Gregorio, B.T., Stroud, R.M., 2011. Origin and evolution of prebiotic organic matter as inferred from the Tagish Lake meteorite. Science 332, 13304–13307.
Herrin, J.S., Zolensky, M.E., Mittlefehldt, D.W., 2010. A carbonaceous chondrite-rich lithology from the HED parent asteroid. PRA 04401. Meteorit. Planet. Sci,. 45 abstract #5438.
Herrin, J.S., Zolensky, M.E., Cartwright, J.A., Mittlefehldt, D.W., Ross, D.K., 2011. Carbonaceous chondrite-rich howardites: the potential for hydrous lithologies on the HED parent. Lunar Planet. Sci. 42 abstract #2806.
Hiroi, T., Pieters, C.M., Zolensky, M.E., Lipschutz, M.E., 1993. Evidence of thermal metamorphism on the C, G, B, and F asteroids. Science 261, 1016–1018.
Hiroi, T., Pieters, C.M., Takeda, H., 1994. Grain size of the surface regolith of asteroid 4 Vesta estimated from its reflectance spectrum in comparison with HED meteorites. Meteoritics 29, 394–396.
Horgan, B.H.N., Cloutis, E.A., Mann, P., Bell III, J.F., 2014. Near-infrared spectra of ferrous minerals and methods for their identification in planetary surface spectra. Icarus 234, 132–154.
Howard, K.T., Benedix, G.K., Bland, P.A., Cressey, G., 2008. Modal mineralogy of Mighei, Nogoya and Cold Bokkeveld CM chondrites by XRD. Meteorit. Planet. Sci. 28 abstract #5160.
Howard, K.T., Benedix, G.K., Bland, P.A., Cressey, G., 2009. Modal mineralogy of CM2 chondrites by X-ray diffraction (PSD-XRD). Part 1: total phyllosilicate abundance and degree of aqueous alteration. Geochim. Cosmochim. Acta 73, 4576–4589.
Howard, K.T., Benedix, G.K., Bland, P.A., Cressey, G., 2010a. Modal mineralogy of CM chondrites by X-ray diffraction (PSD-XRD). Part 2. Degree, nature and settings of aqueous alteration. Geochim. Cosmochim. Acta 75, 2735–2751.
Howard, K.T., Benedix, G.K., Bland, P.A., Cressey, G., 2010b. Aqueous alteration "serpentinization" and the CM-C2ung-CI connection by PSD-XRD. Meteorit. Planet. Sci. 45, A84 Abstract.
Howard, K.T., Alexander, C.M.O'D., Schrader, D.L., Dyl, K.A., 2015. Classification of hydrous meteorites (CR, CM and C2 ungrouped) by phyllosilicate fraction: PSD-XRD modal mineralogy and planetesimal environments. Geochim. Cosmochim. Acta, 149, 206–222.
Izawa, M.R.M., Craig, M.A., Applin, D.M., Sanchez, J.A., Reddy, V., Le Corre, L., Mann, P., Cloutis, E.A., 2015. Variability, absorption features, and parent body searches in "spectrally featureless" meteorite reflectance spectra: case study – Tagish Lake. Icarus 254, 324–332.
Izawa, M.R.M., Cloutis, E.A., Rhind, T., Mertzman, S.A., Poitras, J., Applin, D.M., Mann, P., 2018. Spectral reflectance (0.35-2.5 µm) properties of garnets: implications for remote sensing detection and characterization. Icarus 300, 392–410.
Jenniskens, P., et al., 2012. Radar-enabled recovery of the Sutter's Mill meteorite, a carbonaceous chondrite regolith breccia. Science 338, 1583–1587.
Johnson, T.V., Fanale, F.P., 1973. Optical properties of carbonaceous chondrites and their relationship to asteroids. J. Geophys. Res. 78, 8507–8518.
Kar, A., Sen, A.K., Gupta, R., 2016. Laboratory photometry of regolith analogues: effect of porosity. Icarus 277, 300–310.

Lantz, C., Fornasier, S., Barucci, M., 2013. Statistical Study of Aqueous Alteration on Primitive Asteroids. American Astronomical Society DPS meeting #45, id.205.09.
Lauretta, D.S., 2015. OSIRIS-REx asteroid sample-return mission. In: Pelton, J.N., Allahdadi, F. (Eds.), Handbook of Cosmic Hazards and Planetary Defense. Springer, pp. 543–567.
Lazzaro, D., Barucci, M.A., Perna, D., Jasmin, F.L., Yoshikawa, M., Carvano, J.M.F., 2013. Rotational spectra of (162173) 1999 JU3, the target of the Hayabusa2 mission. Astron. Astrophys. 549, L2.
Lebofsky, L.A., 1978. Asteroid 1 Ceres: evidence for water of hydration. Mon. Not. R. Astron. Soc. 182, 17–21.
Matsuoka, M., Nakamura, T., Kimura, Y., Hiroi, T., Nakamura, R., Okumura, S., Sasaki, S., 2015. Pulse-laser irradiation experiments of Murchison CM2 chondrite for reproducing space weathering on C-type asteroids. Icarus 254, 135–143.
McBride, K., Benedix, G., Welzenbach, L., McCoy, T., 2002. MET 01070; MET 01073; MET 01079. Antarct. Meteorite Newsl. 25 (2), 13–14.
McCord, T.B., Gaffey, M.J., 1974. Asteroids: surface composition from reflectance spectroscopy. Science 186, 352–355.
McCord, T.B., Li, J.-Y, Combe, J.-P., McSween, H.Y., Jaumann, R., Reddy, V., Tosi, F., Williams, D.A., Blewett, D.T., Turrini, D., Palomba, E., Pieters, C.M., De Sanctis, M.C., Ammannito, E., Capria, M.T., Le Corre, L., Longobardo, A., Nathues, A., Mittlefehldt, D.W., Schröder, S.E., Hiesinger, H., Beck, A.W., Capaccioni, F., Carsenty, U., Keller, H.U., Denevi, B.W., Sunshine, J.M., Raymond, C.A., Russell, C.T., 2012. Dark material on Vesta from the infall of carbonaceous volatile-rich material. Nature 491, 83–86.
McCoy, T., Reynolds, V., 2007. PRA 04401; PRA 04402. Antarct. Meteorite Newsl. 30 (1), 16.
Miyamoto, M., 1987. Infrared diffuse reflectances (2.5-25 μm) of some meteorites. Icarus 70, 146–152.
Miyamoto, M., Zolensky, M.E., 1994. Infrared diffuse reflectance spectra of carbonaceous chondrites: amount of hydrous minerals. Meteoritics 29, 849–853.
Miyamoto, M., Mito, A., Takano, Y., 1982. An attempt to reduce the effects of black material from the spectral reflectance of meteorites or asteroids. In: Proceedings of the NIPR Symposium on Antarctic Meteorite, 7, pp. 291–307.
Miyamoto, M., Komatsu, M., Mikouchi, T., 2000. Diffuse reflectance spectra of several chondrites heated at different oxygen fugacities. Lunar Planet. Sci. 31 abstract #1109.
Morlok, A., Bischoff, A., Stephan, T., Floss, C., Zinner, E., Jessberger, E.K., 2006. Brecciation and chemical heterogeneity of CI chondrites. Geochim. Cosmochim. Acta 70, 5371–5394.
Moskovitz, N.A., Abe, S., Pan, K.-S., Osip, D.J., Pefkou, D., Malita, M.D., Elias, M., Kitazato, K., Bus, S.J., DeMeo, F.E., 2013. Rotational characterization of Hayabusa II target asteroid (162173) 1999 JU3. Icarus 224, 24–31.
Nathues, A., Hoffmann, M., Cloutis, E.A., Schäfer, M., Reddy, V., Christensen, U., Sierks, H., Thangjam, G.S., Le Corre, L., Mengel, K., Vincent, J.-P., Russell, C.T., Prettyman, T., Schmedemann, N., Kneissl, T., Raymond, C., Gutierrez-Marques, P., Hall, I., Büttner, I., 2014. Detection of serpentine in exogenic carbonaceous chondrite material on Vesta from Dawn FC data. Icarus 239, 222–237.
Noguchi, T., 1995. Petrology and mineralogy of the PCA 91082 chondrite and its comparison with the Yamato-793495 (CR) chondrite. In: Proceedings of the NIPR Symposium on Antarctic Meteorites, 8, pp. 33–62.
Norton, O.R., 2002. The Cambridge Encyclopedia of Meteorites. Cambridge University Press, Cambridge, UK.
Palomba, E., Longobardo, A., De Sanctis, M.C., Zambon, F., Tosi, F., Ammannito, E., Capaccioni, F., Frigeri, A., Capria, M.T., Cloutis, E.A., Jaumann, R., Combe, J.-P., Raymond, C.A., Russell, C.T., 2014. Composition and mineralogy of dark material units on Vesta. Icarus 240, 58–72.
Pilorget, C., Fernando, J., Ehlmann, B.L., Schmidt, F., Hiroi, T., 2016. Wavelength dependence of scattering properties in the VIS-NIR and links with grain-scale physical and compositional properties. Icarus 267, 296–314.
Popescu, M., Birlan, M., Binzel, R., Vernazza, P., Barucci, A., Nedelcu, D.A., DeMeo, F., Fulchignoni, M., 2011. Spectral properties of eight near-Earth asteroids. Astron. Astrophys. 535 (A15), 15.
Righter, K., 2008. Re-classification of ANSMET samples. Antarct. Meteor. Newsl. 31 (1), 5–8.
Rivkin, A.S., 2012. The fraction of hydrated C-complex asteroids in the asteroid belt from SDSS data. Icarus 221, 744–752.
Rivkin, A.S., Thomas, C.A., Howell, E.S., Emery, J.P., 2015. The Ch-class asteroids: connecting a visible taxonomic class to a 3 μm band shape. Astron. J. 150 (198) (14 pp.).
Rubin, A.E., Trigo-Rodriguez, J.M., Huber, H., Wasson, J.T., 2007. Progressive aqueous alteration of CM carbonaceous chondrites. Geochim. Cosmochim. Acta 71, 2361–2382.
Russell, C.T., Raymond, C.A., 2011. The Dawn mission to Vesta and Ceres. Space Sci. Rev. 163, 3–23.
Salisbury, J.W., Hunt, G.R., Lenhoff, C.J., 1975. Visible and near-infrared spectra: X. Stony meteorites. Mod. Geol. 5, 115–126.
Sanchez, J.A., Reddy, V., Nathues, A., Cloutis, E.A., Mann, P., Hiesinger, H., 2012. Phase reddening on near-Earth asteroids: implications for mineralogical analysis, space weathering and taxonomic classification. Icarus 220, 36–50.
Schröder, S.E., Mottola, S., Carsteny, U., Ciarniello, M., Jaumann, R., Li, J.-Y., Longobardo, A., Palmer, E., Pieters, C., Pruesker, F., Raymond, C.A., Russell, C.T., 2017. Resolved spectrophotometric properties of the Ceres surface from Dawn Framing Camera images. Icarus 288, 201–225.
Shestopalov, D.I., Golubeva, L.F., Cloutis, E.A., 2013. Optical maturation of asteroid surfaces. Icarus 225, 781–793.
Stuart, J.S., Binzel, R.P., 2004. Bias-corrected population, size distribution, and impact hazard for the near-Earth objects. Icarus 170, 295–311.
Takir, D., Emery, J.P., McSween, Jr.H.Y., Hibbitts, C.A., Cralk, R.N., Pearson, N., Wang, A., 2013. Nature and degree of aqueous alteration in CM and CI carbonaceous chondrites. Meteorit. Planet. Sci. 48, 1618–1637.
Takir, D., Clark, B.E., d'Aubigny, C.D., Hergenrother, C.W., Li, J.Y., Lauretta, D.S., Binzel, R.P., 2015. Photometric models of disk-integrated observations of the OSIRIS-REx target Asteroid (101955) Bennu. Icarus 252, 393–399.
Thaisen, K.G., Taylor, L.A., 2009. Meteorite fusion crust variability. Meteorit. Planet. Sci. 44, 871–878.
Tholen, D.J., 1984. Asteroid Taxonomy from Cluster Analysis of Photometry. University of Arizona, Tucson Ph.D. Dissertation.
Trigo-Rodriguez, J.M., Rubin, A.E., Wasson, J.T., 2006. Non-nebular origin of dark mantles around chondrules and inclusions in CM meteorites. Geochim. Cosmochim. Acta 70, 1271–1290.
Tsuda, Y., Yoshikawa, M., Abe, M., Minamino, H., Nakazawa, S., 2013. System design of the Hayabusa 2-asteroid sample return mission to 1999 JU3. Acta Astonautica 91, 356–362.
Vernazza, P., Marsset, M, Beck, P., Binzel, R.P., Birlan, M, Cloutis, E.A., DeMeo, F.E., Dumas, C., Hiroi, T., 2016. Compositional homogeneity of CM parent bodies. Astron. J. 152 (54). doi:10.3847/0004-6256/152/3/54, (10 pp).
Vilas, F., 1994. A cheaper, faster, better way to detect water of hydration on Solar System bodies. Icarus 111, 456–467.
Vilas, F., 2008. Spectral characteristics of Hayabusa 2 near-Earth asteroid targets 162173 1999 JU3 and 2001 QC34. Astrophys. J. 135, 1101–1105.
Vilas, F., Gaffey, M.J., 1989. Phyllosilicate absorption features in main-belt and outer-belt asteroid reflectance spectra. Science 246, 790–792.
Vilas, F., Larson, S.M., Hatch, E.C., Jarvis, K.S., 1993. CCD reflectance spectra of selected asteroids. II. Low albedo asteroid spectra and data extraction techniques. Icarus 105, 67–78.
Zolensky, M.E., Weisberg, M.K., Buchanan, P.C., Mittlefehldt, D.W., 1996. Mineralogy of carbonaceous chondrite clasts in HED achondrites and the Moon. Meteorit. Planet. Sci. 31, 518–537.
Zolensky, M.E., Krot, A.N., Benedix, G., 2008. Record of low-temperature alteration in asteroids. In: MacPherson, G.J., Mittlefehldt, D.W., Jones, J.H. (Eds.), Oxygen in the Solar System. Mineralogical Society of America, pp. 429–462.